



**HAL**  
open science

## **Holocene marine tephra offshore Ecuador and Southern Colombia: First trench-to-arc correlations and implication for magnitude of major eruptions**

Mathilde Bablon, Gueorgui Ratzov, François Nauret, Pablo Samaniego, François Michaud, Marianne Saillard, Jean-noël Proust, Jean-luc Le Penneç, Jean-yves Collot, Jean-Luc Devidal, et al.

### ► To cite this version:

Mathilde Bablon, Gueorgui Ratzov, François Nauret, Pablo Samaniego, François Michaud, et al.. Holocene marine tephra offshore Ecuador and Southern Colombia: First trench-to-arc correlations and implication for magnitude of major eruptions. *Geochemistry, Geophysics, Geosystems*, 2022, 23 (9), pp.e2022GC010466. 10.1029/2022GC010466 . insu-03776996

**HAL Id: insu-03776996**

**<https://insu.hal.science/insu-03776996v1>**

Submitted on 30 Sep 2022

**HAL** is a multi-disciplinary open access archive for the deposit and dissemination of scientific research documents, whether they are published or not. The documents may come from teaching and research institutions in France or abroad, or from public or private research centers.

L'archive ouverte pluridisciplinaire **HAL**, est destinée au dépôt et à la diffusion de documents scientifiques de niveau recherche, publiés ou non, émanant des établissements d'enseignement et de recherche français ou étrangers, des laboratoires publics ou privés.



Distributed under a Creative Commons Attribution - NonCommercial 4.0 International License



## RESEARCH ARTICLE

10.1029/2022GC010466

### Key Points:

- We propose a first land-sea correlation of distal Holocene tephra off Ecuador based on <sup>14</sup>C age and geochemical data
- Products from at least seven explosive Holocene eruptions in Ecuador and south Colombia reached the Pacific Ocean
- Volumes of tephra emitted by largest eruptions vary between 1.3 and 6.0 km<sup>3</sup>, suggesting they were VEI-5 eruptions

### Supporting Information:

Supporting Information may be found in the online version of this article.

### Correspondence to:

M. Bablon,  
[mathilde.bablon@geoazur.unice.fr](mailto:mathilde.bablon@geoazur.unice.fr)

### Citation:

Bablon, M., Ratzov, G., Nauret, F., Samaniego, P., Michaud, F., Saillard, M., et al. (2022). Holocene marine tephra offshore Ecuador and Southern Colombia: First trench-to-arc correlations and implication for magnitude of major eruptions. *Geochemistry, Geophysics, Geosystems*, 23, e2022GC010466. <https://doi.org/10.1029/2022GC010466>

Received 5 APR 2022

Accepted 20 JUL 2022

### Author Contributions:

**Funding acquisition:** Mathilde Bablon, Gueorgui Ratzov, François Michaud, Marianne Saillard, Jean-Noël Proust

**Investigation:** Mathilde Bablon, Gueorgui Ratzov, François Nauret, Pablo Samaniego, François Michaud, Marianne Saillard, Jean-Noël Proust, Jean-Luc Le Pennec, Jean-Luc Devidal, François Orange, Céline Liorzou, Sébastien Migeon, Silvia Vallejo, Patricia Mothes, Miguel Gonzalez

**Methodology:** Mathilde Bablon

© 2022. The Authors.

This is an open access article under the terms of the [Creative Commons Attribution-NonCommercial License](https://creativecommons.org/licenses/by/4.0/), which permits use, distribution and reproduction in any medium, provided the original work is properly cited and is not used for commercial purposes.

# Holocene Marine Tephra Offshore Ecuador and Southern Colombia: First Trench-to-Arc Correlations and Implication for Magnitude of Major Eruptions

Mathilde Bablon<sup>1,2</sup> , Gueorgui Ratzov<sup>1</sup> , François Nauret<sup>3</sup>, Pablo Samaniego<sup>3</sup> , François Michaud<sup>4</sup>, Marianne Saillard<sup>1</sup> , Jean-Noël Proust<sup>5</sup> , Jean-Luc Le Pennec<sup>6,7</sup>, Jean-Yves Collot<sup>1</sup> , Jean-Luc Devidal<sup>3</sup>, François Orange<sup>8</sup>, Céline Liorzou<sup>6</sup> , Sébastien Migeon<sup>4</sup>, Silvia Vallejo<sup>9</sup>, Silvana Hidalgo<sup>9</sup> , Patricia Mothes<sup>9</sup> , and Miguel Gonzalez<sup>10</sup>

<sup>1</sup>Université Côte d'Azur, CNRS, IRD, Observatoire de la Côte d'Azur, Valbonne, France, <sup>2</sup>ISTerre, IRD, CNRS, OSUG, Université Grenoble Alpes, Saint-Martin-d'Hères, France, <sup>3</sup>Laboratoire Magmas et Volcans, Université Clermont Auvergne, CNRS, IRD, OPGC, Clermont-Ferrand, France, <sup>4</sup>Université Côte d'Azur, Sorbonne Universités, CNRS, Observatoire de la Côte d'Azur, IRD, Valbonne, France, <sup>5</sup>Université Rennes 1, CNRS, Géosciences Rennes, Rennes, France, <sup>6</sup>Université de Bretagne Occidentale, laboratoire Geo-Océan, CNRS-UBO-Ifremer-UBS, IUEM, Plouzané, France, <sup>7</sup>IRD Office for Indonesia & Timor Leste, Jakarta, Indonesia, <sup>8</sup>Université Côte d'Azur, Centre Commun de Microscopie Appliquée, Nice, France, <sup>9</sup>Instituto Geofísico, Escuela Politécnica Nacional, Quito, Ecuador, <sup>10</sup>Escuela Superior Politecnica del Litoral (ESPOL), Grupo de Investigación en Geociencias Marinas y Costeras (GEMAC), FIMCM-FICT, Campus Gustavo Galindo, Guayaquil, Ecuador

**Abstract** Tephra layers preserved in marine sediments are strong tools to study the frequency, magnitude and source of past major explosive eruptions. Thirty-seven volcanoes from the Ecuadorian and Colombian arc, in the northern Andes, experienced at least one eruption during the Holocene. The volcanic hazard is therefore particularly high for the populated areas of the Andes and in particular cases for the coastal region, and it is crucial to document such events to improve hazard assessment. The age and distribution of deposits from major Holocene eruptions have been studied in the Cordillera, but no descriptions of distal fallouts have been published. In this study, we focused on 28 Holocene tephra layers recorded in marine sediment cores collected along the northern Ecuador—Southern Colombia margin. New lithological, geochemical and isotope data together with <sup>14</sup>C datings on foraminifers allow us to determine the age and volcanic source of marine tephra, and to propose a first land-sea correlation of distal tephra fallouts. We show that at least seven explosive eruptions from Guagua Pichincha, Atacazo-Ninahuilca, Cotopaxi, and Cerro Machín volcanoes left tephra deposits recorded in marine cores over 250 km away from their source. Volume estimates of emitted tephra range between 1.3 and 6.0 km<sup>3</sup> for the tenth century Guagua Pichincha, ~5 ka Atacazo-Ninahuilca, ~6.7 and ~7.9 ka Cotopaxi events, suggesting that they were eruptions of Volcanic Explosivity Index of 5. The distribution of these deposits also brings new constraints for a better evaluation of the volcanic hazard in Ecuador.

**Plain Language Summary** During major explosive eruptions, large volumes of gases and tephra (lapilli and ash particles) are thrown into the atmosphere and can be spread by winds over 100 km and more. Tephra fallouts can impact the population, infrastructures and climate. It is therefore essential to document the age and magnitude of past major eruptions to better assess the volcanic hazards. In this study, we use the mineralogy, glass shard morphology, and the geochemical composition of tephra settled in marine sediments off Ecuador and Colombia to investigate their source. Thickness of tephra layers and radiocarbon ages performed on under- and over-lying marine fauna allow us to determine the age of the eruptions, whereas the distribution of tephra yields constraints on the volume of fallout deposits. We show that the largest explosive eruptions from Ecuadorian and Colombian volcanoes reached the Pacific Ocean with a recurrence rate of about 1.5 events per millennium over the past 8 kyr.

## 1. Introduction

Large explosive eruptions present a significant hazard to populations and infrastructures. Indeed, during such events, large volumes of tephra and volatiles are ejected into the atmosphere and can be spread over thousands of square kilometers, affecting surrounding areas and the regional climate, as for the 79 CE Vesuvius (Barbante

**Project Administration:** Mathilde Bablon

**Writing – original draft:** Mathilde Bablon

**Writing – review & editing:** Mathilde Bablon, Gueorgui Ratzov, François Nauret, Pablo Samaniego, François Michaud, Marianne Saillard, Jean-Noël Proust, Jean-Luc Le Pennec, Jean-Yves Collot, Jean-Luc Devidal, François Orange, Céline Liorzou, Silvia Vallejo, Silvana Hidalgo

et al., 2013; Vogel & Märker, 2013) and 1991 Pinatubo (Bluth et al., 1992) eruptions. Determining the age, magnitude, and extent of past major volcanic events is crucial to document the recurrence rate of eruptions, the distribution of deposits, and the volume of released material. These data contribute to better assess the current volcanic hazard. Providing reliable temporal and stratigraphic constraints on terrestrial and marine sedimentary archives, the study of tephra deposits is helpful in paleoseismology, tectonics, sedimentology, paleoclimatology or archeology. For instance, offshore Kamchatka peninsula and New Zealand, in the Aegean Sea and in the Lake Petén Itzá (northern Guatemala), the age model of marine tephra allows quantifying the recurrence rate of past eruptions, to correlate them with terrestrial deposits, to date marine sediments, to establish sedimentation rate models, and to constrain magnitude of past eruptions (Derkachev et al., 2020; Hopkins et al., 2020; Kutterolf, Freundt, Druitt, et al., 2021; Kutterolf et al., 2016). Tephrochronology allowed estimating the marine surface reservoir radiocarbon age during the last deglaciation offshore Chile (Siani et al., 2013), dating ice-rafted debris deposition offshore Iceland (Lacasse and van den Bogaard, 2002), and investigating the climate/volcanism interaction at Izu-Bonin arc (Schindlbeck et al., 2018).

This paper documents major Holocene eruptions of the Ecuadorian and south Colombian arc, located in the northern Andes. In this study, we provide (a) new information on the sedimentary facies, mineral assemblage, major and trace element content of glass shards, and Sr-Pb isotope ratios of tephra layers recorded in marine sediment cores collected during the *Amadeus* and *Atacames* oceanographic campaigns (R/V *L'Atalante*; Collot et al., 2005; Michaud et al., 2015) along the Ecuadorian margin to identify their source by comparing their fingerprint with proximal products of major Holocene eruptions, (b) a regional correlation of tephra layers that allows to improve isopach maps to better estimate the magnitude of major explosive events and to infer future hazard, and (c) new  $^{14}\text{C}$  ages for marine sedimentary sequences, that refine the age models deduced from available  $^{14}\text{C}$  data, strengthen the characterization of the deposits of each eruption, and thus provide reliable stratigraphic markers for subsequent investigations.

## 2. Geological Context

### 2.1. Regional Setting

The Northern Volcanic Zone of the Andes originates from the eastward dipping subduction of the oceanic Nazca plate beneath the continental South American plate (e.g., Barberi et al., 1988) at a present-day convergence rate of  $5.6 \text{ cm yr}^{-1}$  (Nocquet et al., 2014). It includes volcanoes from Ecuador and Colombia (Figure 1a). They are distributed along the Eastern and Western Cordilleras, in the Interandean Valley, and in the Sub-Andean Zone in Ecuador, whereas they form a single row along the Cordillera Central in Colombia (Figure 1a; e.g., Barberi et al., 1988; Hall & Wood, 1985; Hall et al., 2008). The origin of such distribution is debated, but may be explained by downgoing slab geometry, the structural inheritance and crustal faults, the tectonic activity, and the eastward subduction of the Carnegie Ridge (blue dashed line; Figure 1a) between  $\sim 0^\circ$  and  $2^\circ\text{S}$  (e.g., Bablon, Quidelleur, Samaniego, et al., 2020; Martin et al., 2014). The latter is inferred to strongly affect submarine morphologies by the subduction of the topographically irregular Carnegie Ridge (e.g., Collot et al., 2009, 2017; Graindorge et al., 2004; Hernandez et al., 2020; Lonsdale, 1978; Proust et al., 2016) and coastal morphologies by emerged Pleistocene terraces along the central and northern Ecuadorian coast (Pedoja et al., 2006). An inland uplift of the Coastal Cordillera (Brichau et al., 2021, Figure 1a) resulted in the main river divide in near latitude  $0^\circ$  (Collot et al., 2004; Reyes, 2013). The Coastal Cordillera deflects the Andean drainage systems toward the Esmeraldas canyon to the north, and the Guayas river to the south (Figure 1a; Lonsdale, 1978; Collot et al., 2009). The sediment supply offshore Central Ecuador is therefore limited, and mainly comes from the Coastal Cordillera.

### 2.2. Morphology and Sedimentation of the Margin

Our study area extends from the north of the Gulf of Guayaquil to the Patia submarine canyon offshore southern Colombia. Offshore Ecuador, the margin is characterized by three distinct segments with a relatively simple morphology, composed by a shelf, a continental slope, and a small frontal wedge (Collot et al., 2009). Where the Carnegie Ridge underthrusts the margin ( $0^\circ$ – $2^\circ\text{S}$ ), the trench has been uplifted, resulting in no trench basin, and limited slope basins (Lonsdale, 1978). Numerous morphological indents at the present-day seafloor are interpreted as scars left by slope failures subsequent to the subduction of seamounts (Collot et al., 2005, 2017; Marcaillou et al., 2016; Proust et al., 2016; Sage et al., 2006).

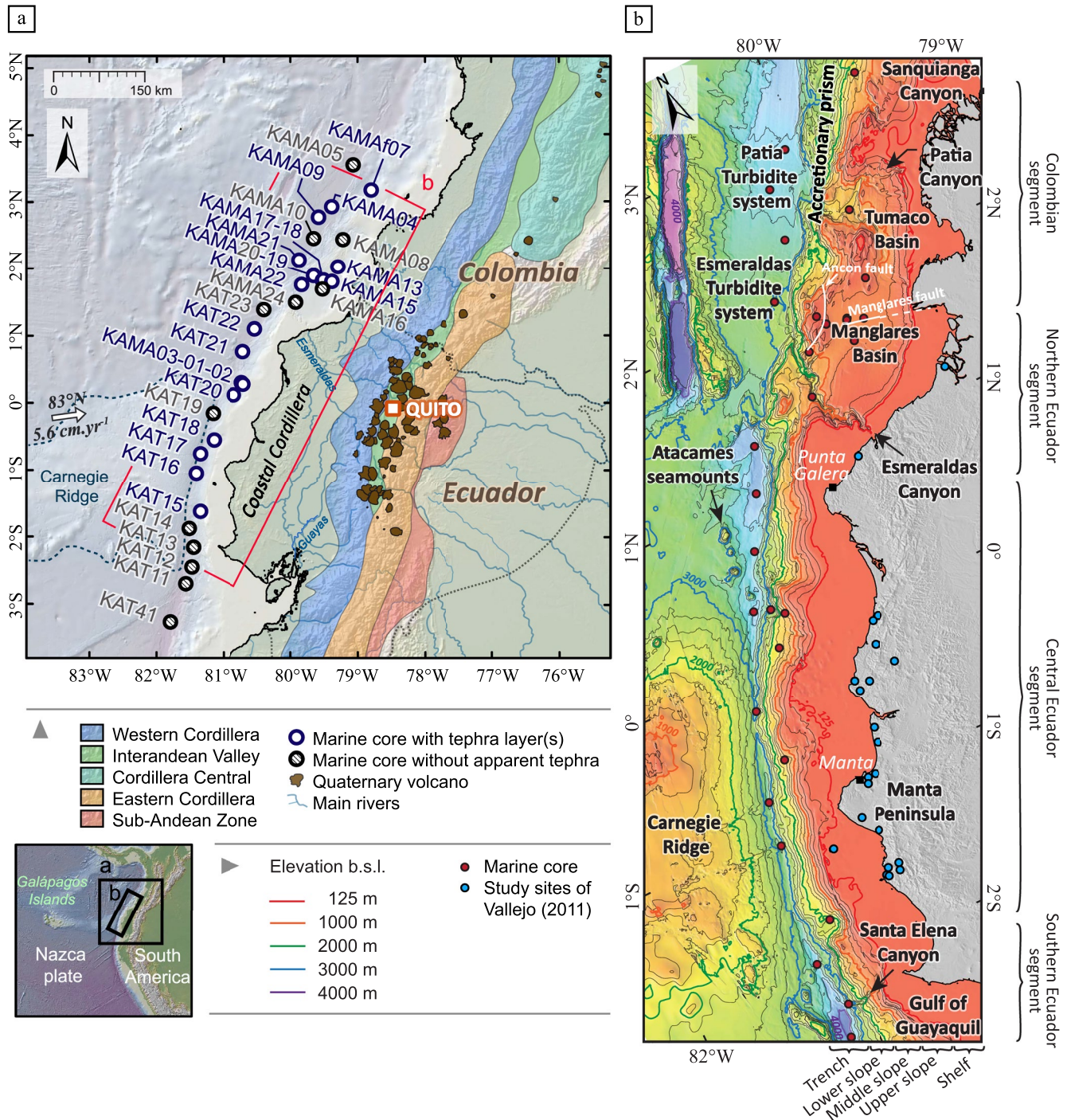


**Figure 1.** Geological context of the northern Andes in Ecuador and Southern Colombia. (a) Main geological zones (modified from Ancellin et al. (2017)), and location of marine sedimentary cores (blue and dashed circles) collected during the *Amadeus* (2005) and *Atacames* (2012) oceanographic cruises and analyzed in this study. White arrow indicates the direction of the Nazca plate motion relative to South America (Nocquet et al., 2014). The Carnegie Ridge corresponds to the trace of the Galápagos hotspot activity on the Nazca plate. (b) Bathymetry of the Ecuador-south Colombia trench obtained from multi-beam bathymetric data (150-m resolution; Michaud et al., 2006). B.s.l.: below sea level.

### 2.2.1. Western Colombia Accretionary Wedge Piggyback Basin

Northward from the Esmeraldas River and offshore Southern Colombia, the subduction is dominated by tectonic accretion (Collot et al., 2004; Marcaillou et al., 2008), drastically changing the submarine morphology: an

accretionary prism develops at the margin front (Mountney & Westbrook, 1997), that bounds the Manglares and Tumaco forearc basins (Marcaillou & Collot, 2008, Figure 1b). The subduction trench is wider and filled up by ~3,000 m of deposits (Collot et al., 2008) delivered by the Esmeraldas and Mira/Patia Submarine canyons (Collot et al., 2019; Marcaillou et al., 2008; Ratzov et al., 2012; Figure 1b).

At the northern boundary of the studied area, a 2,800 m-deep piggyback basin associated with the Colombian accretionary wedge was likely fed by the Sanquinga Canyon (Collot et al., 2009; Marcaillou & Collot, 2008). Sedimentary core KAMAF07 collected at the northern tip of the basin (Figures 1a and 1b) reveals a stack of silty to sandy turbidites, interbedded with hemipelagic mud (Ratzov, 2009). The strong bioturbation along the core suggests low sedimentation rate, compatible with an inactive canyon.

### 2.2.2. Esmeraldas and Patia Trench Sedimentary Systems

South of the Sanquinga Canyon, turbidite accumulations formed at the mouth of both the Esmeraldas Canyon (cores KAMA09, 10 and 21, Figure 1a; Migeon et al., 2017) and the Patia Canyon (core KAMA04; Ratzov, 2009; Ratzov et al., 2012) and supply the trench with significant amounts of sediments. The latter consists of Mass Transport Deposits (MTDs) and an alternation of silty- to coarse sandy-turbidite layers, most of which present a sharp and erosive base, interbedded with detritic or hemipelagic mud. Based on the sediment content and sedimentary structures of the trench deposits, the above authors infer a provenance either from (a) a direct input from the rivers during major floods or El Niño events, or (b) slope failures on the canyon walls during large magnitude earthquakes (Migeon et al., 2017).

### 2.2.3. Manglares and Tumaco Forearc Basins

The cores collected in the Manglares forearc basin (KAMA15 to 19; Figures 1a and 1b) mostly contain fine-grained and silty clays, alternating with a few coarser silts to fine-grained sands with cm-thick fining upward beds. These deposits are interpreted as the decantation of hemipelagic sedimentation interbedded with a limited amount of fine-grained turbidites (Ratzov, 2009). Pinpointing the boundary of each layer is difficult due to the sediment homogeneity and intense bioturbation.

### 2.2.4. Ecuadorian Shelf and Upper Slope

Shelf and upper slope deposits show alternation of massive bioclastic silty sands and clayey to sandy silts interpreted as current- and storm-swept seafloor environment (Proust et al., 2016). We found no tephra records in cores from the shelf and upper slope.

### 2.2.5. Ecuadorian Trench and Slope Basins

Trench and slope basin deposits (cores KAT11 to 21, KAT41, KAMA01, and KAMA03; Figures 1a and 1b) show similarities in their sedimentary record. They contain MTDs, and mostly muddy and few sandy turbidites (Gonzalez, 2018; Lonsdale, 1978; Ratzov et al., 2010), which are fine-grained when compared to those retrieved in the Esmeraldas and Patia sedimentary systems. Only few hemipelagites are observed, and distinguishing them from turbidite muddy tails proves difficult because of the similarities in term of grain size and facies between these beds. Because of their mineralogical and faunal contents, and the presence of numerous scars on the margin seafloor, most of the turbidites should result from remobilization of the margin slope. The two main canyons (Santa Elena and Guayaquil, Figure 1) that are cutting the slope do not incise the seafloor upstream of the shelf break. Canyons were therefore likely active during sea-level lowstands, when they were directly connected to feeding rivers (Collot et al., 2009; Coronel, 2002; Loayza et al., 2013; Michaud et al., 2015; Witt et al., 2006). Therefore, their contribution to the trench deposits was probably low during the Holocene sea-level highstand. In the trench, only few turbidites originate from the failure of the pelagic cover of the downgoing plate (Gonzalez, 2018; Ratzov, 2009). The sedimentary beds are bioturbated, attesting of a relatively low accumulation rate, with Late Pleistocene to Holocene deposits. Seafloor scours along the Ecuador trench attest of the northward flow of bottom currents that accelerate where the trench is shallowest and forms a pass (Lonsdale, 1977), and could account for sediment dispersal away from the trench.

## 2.3. Volcanic Activity

The Ecuadorian arc is composed of 76 volcanic edifices active during the Quaternary (e.g., Hall et al., 2008; Ramón et al., 2021). Their distribution over a restricted area (~300 km-long [NS] and maximum 110 km-wide

[E-W]; Figure 1a) makes it the highest volcanic density number in the Andes (Hall et al., 2008; Martin et al., 2014). The oldest dated volcanic deposits of the arc originate from the Chacana caldera (2.6 Ma; Opdyke et al., 2006), and the Atacazo, Pichincha, and Cayambe (Figure 2a) volcanic complexes (1.3–1.1 Ma; Hidalgo, 2006; Robin et al., 2010; Samaniego et al., 2005). The volcanic activity has seemingly intensified over the last 500 kyr. This may have been caused by changes in the deep slab geometry and a magma rise favored by the activation of major crustal faults (Bablon et al., 2019). Twenty-four volcanoes were active during the Holocene (e.g., Ramón et al., 2021), and eight of them experienced at least one eruption within the last 500 years (e.g., Bernard & Andrade, 2011; Hall et al., 2008). About 15 volcanoes in the Colombian arc erupted during the Holocene, with a sustained activity for Galeras and Azufral volcanoes (Hall & Mothes, 2008c).

Subduction zone volcanism is often characterized by large explosive events, associated with the formation of high eruption columns of tephra and volatiles. In Ecuador and Colombia, products from such major eruptions that reach the stratosphere are mostly distributed to the west of the Andean arc due to the persistent westward winds. Depending on the eruption magnitude and the wind velocity and direction, some ash clouds from these events can reach the coastal plain and the Pacific Ocean. Several Holocene tephra layers have been identified along the Ecuadorian trench (Gonzalez, 2018; Ratzov, 2009) and on the coastal region (Vallejo Vargas, 2011; Zeidler & Pearsall, 1994).

In this study, we focus on tephra layers recorded in Holocene sedimentary sequences, and therefore on major Holocene eruptions, whose Volcanic Explosivity Index (VEI) inferred from bulk tephra volume estimates are ranked at four or more on the scale of Newhall and Self (1982). A short description of the eruptive history of Ecuadorian and Colombian volcanoes that experienced at least one major eruption during the Holocene, as well as main eruptions whose products may have reached the coastal region during the Holocene, are given in Table 1, from the south to the north (green volcanoes; Figure 2a). Other volcanoes were active during the Holocene, such as Antisana, Cayambe, Chacana, Chachimbiro, Chimborazo, Iliniza, Imbabura, Fuya Fuya, Reventador, Sangay, and Sumaco in Ecuador and Cerro Bravo, Chiles-Cerro Negro, Cumbal, Doña Juana, Nevado del Huila, Nevado del Tolima, Petacas, Puracé, Romeral, Santa Isabel, and Sotará in Colombia, but we found no evidences in this study of any powerful eruption from these edifices.

#### 2.4. Geochemistry of Magmas From the North Andean Arc

Major and trace elements contents of glass shards can be used to identify the source of distal products (e.g., Derkachev et al., 2020; Lowe, 2011). As the Ecuadorian and Colombian arcs correspond to subduction zone volcanism, magmas generally belong to the medium-K calc-alkaline series (e.g., Hall et al., 2008). Andesite and dacite constitute the dominant rock type, with rare basaltic andesites and rhyolites. The geochemistry of magmas is typical of subduction volcanism, with enrichments in Large-Ion Lithophile Elements (LILE, such as Rb, Ba, and K) and in Light Rare-Earth Elements (LREE, such as La, Ce, and Nd) compared to Heavy Rare-Earth Elements (HREE, such as Dy, Er, and Yb), and depletions in High Field Strength Elements, notably Zr, Th, Nb, and Ta (e.g., Ancellin et al., 2017; Hidalgo et al., 2012). The geochemical signature of volcanoes depends on their position within the arc. The content of most of the incompatible elements (Ba, Nb, Th, Y, Rb, Sr, Zr, and Rare Earth Elements, for instance) increases with the distance from the trench, whereas the ratios of fluid-mobile to fluid-immobile elements decrease (Ba/Th, Ba/La, and Ba/Nb, for instance), being interpreted as a lower degree of mantle partial melting (e.g., Ancellin et al., 2017; Hidalgo et al., 2012). As a result, edifices from southern Colombia and from the volcanic front of the Ecuadorian arc are characterized by low-K magmatic series and lower LREE contents, whereas back-arc volcanoes from the Sub-Andean Zone (Figure 1a) are distinguished by shoshonitic lavas, less differentiated and more enriched in alkaline elements (e.g., Ancellin et al., 2017; Hidalgo et al., 2012). In addition, several studies focused on magmatic products emitted during the recent major eruptions, and described the mineral assemblage and the geochemical composition of Holocene products, as for Cotopaxi (e.g., Hall & Mothes, 2008b), Atacazo-Ninahuilca (Hidalgo et al., 2008), and Guagua Pichincha (Samaniego et al., 2010) volcanoes.

At the scale of the Ecuadorian arc, isotope ratios of Pb vary over different fields. Volcanoes from the southern half of the arc and the Western Cordillera (Figure 1a) are mainly characterized by high  $^{206}\text{Pb}/^{204}\text{Pb}$  and  $^{207}\text{Pb}/^{204}\text{Pb}$  ratios ( $\sim 19$  and  $>15.63$ , respectively; Ancellin et al., 2017), whereas volcanoes located north of the Eastern Cordillera and in the Sub-Andean Zone (Figure 1a) have the highest ( $>19$ ) and the lowest ( $<18.8$ )  $^{206}\text{Pb}/^{204}\text{Pb}$ , respectively. In addition, isotope ratios of Sr, Nd, and O show an across- and along-arc zonation (e.g., Ancellin et al., 2017; Hidalgo et al., 2012). Volcanoes located in the northern part of the Eastern Cordillera are characterized by the lowest  $^{87}\text{Sr}/^{86}\text{Sr}$  and the highest  $^{143}\text{Nd}/^{144}\text{Nd}$  ratios ( $<0.7039$  and  $>0.5129$ , respectively), whereas they present a low  $^{87}\text{Sr}/^{86}\text{Sr}$  and

**Table 1**  
Age, Mineral Assemblage, Volcanic Explosivity Index (VEI), and Plume Direction of Major Holocene Eruptions (VEI ≥ 4), Whose Products May Have Reached the Pacific Ocean

Volcano	Coordinates (lat.-long.)	Elevation (m a.s.l.)	Location	Eruptive history	Major Holocene eruption	Age (cal BP)	Characteristics	VEI	Plume direction	Source
Tungurahua	1.47°S–78.44°W	5,023	Ecuador—Eastern Cordillera	The eruptive history of Tungurahua volcano is well documented, as it is one of the most active volcanoes in Ecuador. Its construction started at about 300 ka, and the volcano was recently erupting between 1999 and 2016. Tephra layers and pyroclastic deposits indicate that it experienced several explosive eruptions during the past 30 kyr, and at least one VEI-3 event per century since the thirteenth century	Blast explosion associated with flank collapse	~3050	Scoria bombs within a lahar deposit that immediately followed the avalanche indicate that an eruptive event either triggered or accompanied the sector collapse event	5	NW	Hall et al. (1999); Guillaume-Gentil (2008); Le Pennec et al. (2008, 2013); and Bablon et al. (2018)
Quilotoa	0.85°S–78.90°W	3,914	Ecuador—Western Cordillera	Quilotoa volcano is the most-western active volcano of the Ecuadorian arc (Figure 2a). It experienced at least eight explosive events since ~215 ka, as evidenced by thick ash falls, pumice falls and surge deposits	~800 BP	690–730 3100–3250	Stratigraphic marker for the southern termination of the Ecuadorian arc covering an area of ~810 000 km <sup>2</sup> . Proximal tephra layer contains many small golden biotite, plagioclase, and amphibole crystals	6	W-NW	Rosi et al. (2004); Mothes and Hall (2008); Guillaume-Gentil (2008); and Vallejo Vargas (2011)

**Table 1**  
*Continued*

Volcano	Coordinates (lat.-long.)	Elevation (m a.s.l.)	Location	Eruptive history	Major Holocene eruption	Age (cal BP)	Characteristics	VEI	Plume direction	Source
Cotopaxi	0.68°S–78.44°W	5,911	Ecuador— Eastern Cordillera	Cotopaxi volcano is one of the highest edifices of Ecuador. Its eruptive history is divided into three periods, which correspond to Cotopaxi I, IIA and IIB stages. Cotopaxi I corresponds to the construction of rhyolitic domes between ~560 and ~215 ka, and is followed by an apparent ~200 kyr quiescence period. Cotopaxi IIA is characterized by a series of five major rhyolitic episodes (called “F series”) that occurred between ~13 and ~5 ka, evidenced by pumiceous tephra falls, ash flows and debris flows. This sequence is followed by the Colorado Canyon rhyolite episode, the strongest and last Holocene explosive phase of Cotopaxi. It led to a large pyroclastic flow that crops out on the northern flank of the volcano. Cotopaxi IIB corresponds to the late Holocene andesite episode. It is marked by a small rhyolitic episode at ~2.1 ka and at least 19 andesitic eruptive cycles from 4 ka until the present, with an increase of the frequency over time	Colorado Canyon	4410–5320	Pumice lapilli fall deposits contain plagioclase and quartz crystals, with magnetite and biotite crystals in smaller proportions. Geochemical signature is closer to Chalupas products	4		Barberi et al. (1995); Hall and Mothes (2008b); and Vallejo Vargas (2011)
					F4	6550–6800	Largest events of the “F rhyolitic series,” with volumes estimated at about 5 and 8 km <sup>3</sup> , respectively. Pumice lapilli layers carry plagioclase, biotite, pyroxene and quartz crystals, as well as oxides	5	SW-NW	
					F2	7160–8600		5–6	SW-NW	

(Continued)



Table 1  
Continued

Volcano	Coordinates (lat.-long.)	Elevation (m a.s.l.)	Location	Eruptive history	Major Holocene eruption	Age (cal BP)	Characteristics	VEI	Plume direction	Source
Atacazo-Ninahuilca	0.35°S–78.62°W	4,463	Ecuador—Western Cordillera	Atacazo-Ninahuilca volcanic complex is located 10 km southwest of Quito (Figure 2a). It is made up of three edifices. The oldest one, La Caracacha, is an andesitic volcano that was active about 1.29 Ma. After a quiescence period, the construction of Atacazo volcano started at ~200 ka and ended with satellite dome extrusions at ~70 ka. Ninahuilca corresponds to the youngest edifice, and experienced at least six periods of explosive activity (called “N1 to N6”) triggered by the construction of a dome, and evidenced by thick tephra layers and pyroclastic flow deposits. Radiocarbon ages indicate that N3, N4, N5, and N6 events occurred at ~9950, ~6200, ~4950, and ~2300 cal BP, respectively	N6 N5 N4	2220–2240 4880–4940 6140–6310	Onland tephra layers are made up of pumices, fragmented lithics and ash, which contain glass shards and crystals (plagioclase, pyroxene and Fe-Ti oxides for N2 and N3, plagioclase and quartz for N4, and plagioclase and amphibole for N5 and N6 events)	5 5	W	Hidalgo (2006); Hidalgo et al. (2008); Guillaume-Gentil (2008); and Vallejo Vargas (2011)
Pichincha	0.17°S–78.60°W	4,784	Ecuador—Western Cordillera	North of Atacazo, Pichincha volcanic complex comprises the old Rucu Pichincha, whose eruptive history spanned between 1.1 Ma and ~150 ka, and the young Pichincha, whose construction started between ~60 and 22 ka with lava flows and dome extrusions. It experienced four main eruptive phases with major Plinian eruptions during the last 3 kyr. Radiocarbon ages performed on resulting tephra fall and pyroclastic flow deposits indicate that those explosive events occurred at ~3200, ~1900, ~1000 and ~400 cal BP	Tenth century Oldest Holocene deposits	960–1000 3890–3930	Proximal products of the ~1000 cal BP event consist in ash, lapilli and pumice fall layers. Pumices contain plagioclase and amphibole phenocrysts with abundant oxidized xenoliths from the basement  Blocks of proximal pyroclastic flows are andesites to dacites with a mineral assemblage of plagioclase, hornblende, orthopyroxene crystals, and Fe–Ti oxides	5	NNW  SW	Robin et al. (2008, 2010); and Vallejo Vargas (2011)

**Table 1**  
*Continued*

Volcano	Coordinates (lat.-long.)	Elevation (m a.s.l.)	Location	Eruptive history	Major Holocene eruption	Age (cal BP)	Characteristics	VEI	Plume direction	Source
Pululahua	0.04°S–78 .46°W	3,356	Ecuador— Western Cordillera	Pululahua is a potentially active dome complex whose oldest known activity is dated at 18 ± 3 ka. At least four explosive eruptive events occurred between 2595–2495 and 2350–2335 cal BP leading to thick succession of pumice-rich tephra fall and pyroclastic density current deposits around Pululahua. The last and smaller event occurred at 2251–2160 cal BP with the extrusion of Rumiloma and Pondoña pelean domes	Four explosive eruptive phases of Unit III	2335–2600	Proximal pumices contain abundant zoned plagioclase phenocrysts, as well as amphibole and pyroxene crystals	4	SW	Papale and Rosi (1993); Vallejo Vargas (2011); and Andrade et al. (2021)
Cuicocha	0.31°N–78 .36°W	3,246	Ecuador— Western Cordillera	Cuicocha caldera is located 50 km north of Quito, at the southern foot of Cotacachi volcano (Figure 2a). This depression, presently filled by a lake, is a remnant of a large explosive eruption that took place after a dome destruction ~3000 cal BP, based on radiocarbon ages performed on the associated pyroclastic density current deposits	~3100 BP eruption	3150–3210	Proximal products contain alkali feldspars, amphibole and biotite crystals		WNW-SSW	Hall and Mothes (1994); Guillaume-Gentil (2008); Vallejo Vargas (2011); Almeida (2016)
Soche	0.55°N–77 .58°W	3,955	Ecuador— Eastern Cordillera	South of the Colombian border (Figure 2a), the eruptive history of Soche volcano is poorly documented. A Plinian eruption occurred about 9600 cal BP, based on radiocarbon ages of the thick pumice-rich pyroclastic flows deposited in the Ecuadorian and Colombian Interandean Valley (green field, Figure 1a)	Last major eruption	9482–9700		5	W	Beate (1994); and Hall and Mothes (2008c)
Azufra	1.08°N–77 .68°W	4,070	Colombia	The eruptive history of Zufra volcano, immediately north of the Ecuadorian border (Figure 2a), is poorly known. Its summit caldera is truncated by a Holocene lava dome complex and is surrounded by six units of surge and pyroclastic deposits emitted at about 18000, 4050, 3900, 3700, 3500, and 300 cal BP						Williams et al. (2017); and Castilla et al. (2019)

(Continued)

**Table 1**  
*Continued*

Volcano	Coordinates (lat.-long.)	Elevation (m a.s.l.)	Location	Eruptive history	Major Holocene eruption	Age (cal BP)	Characteristics	VEI	Plume direction	Source
Galeras	1.22°N–77.37°W	4,276	Colombia	Galeras volcanic complex has been active since at least ~800 ka. It experienced a complex history with several construction and destruction stages producing thick pyroclastic and debris avalanche deposits. However, the six eruptive periods that occurred during the last 4.5 kyr have been of small scale						Calvache et al. (1997)
Cerro Machín	4.49°N–75.39°W	2,749	Colombia	Located 150 km southwest of Bogotá, Cerro Machín is one of the most dangerous active volcanoes of Colombia. It experienced at least six major Plinian eruptions during the Holocene, associated with thick pyroclastic flows, pyroclastic surges, pyroclastic falls and lahars.	Major events were dated at about 5000, 4600, 3600, 2600, 1200, and 900 years BP for the Espartillal, P0, P1, Guatico, P2 and Anillo units respectively		Proximal ignimbrites contain quartz-dacite pumice (50%), lithics (30%, mostly metamorphic xenoliths) and ash. Lava dome dacites contain plagioclase, quartz, and amphibole crystals with some biotite and scarce Fe-Ti oxides, olivine, apatite and pyroxene crystals	W and S	Thouret (1995); Rueda (2005); Murcia et al. (2008); and Laeger et al. (2013)	
Nevado Del Ruiz	4.89°N–75.32°W	5,279	Colombia	The Nevado Del Ruiz volcano comprises a high and well-known volcanic hazard potential due to lahars generated by interactions between magma and summit ice cover. Its volcanic history is characterized by alternating construction and collapse periods. The oldest edifice was active between 1.8 and 1.0 Ma, and partially collapsed between 1.0 and 0.8 Ma. A second edifice grown between 800 and 150 ka. The activity of the present active edifice is highly explosive, with at least 12 explosive events during the Holocene, and associated with the growth of summit domes						Thouret et al. (1990)

Note. Age calibrations are detailed in Data Set S1. A.s.l.: above sea level.

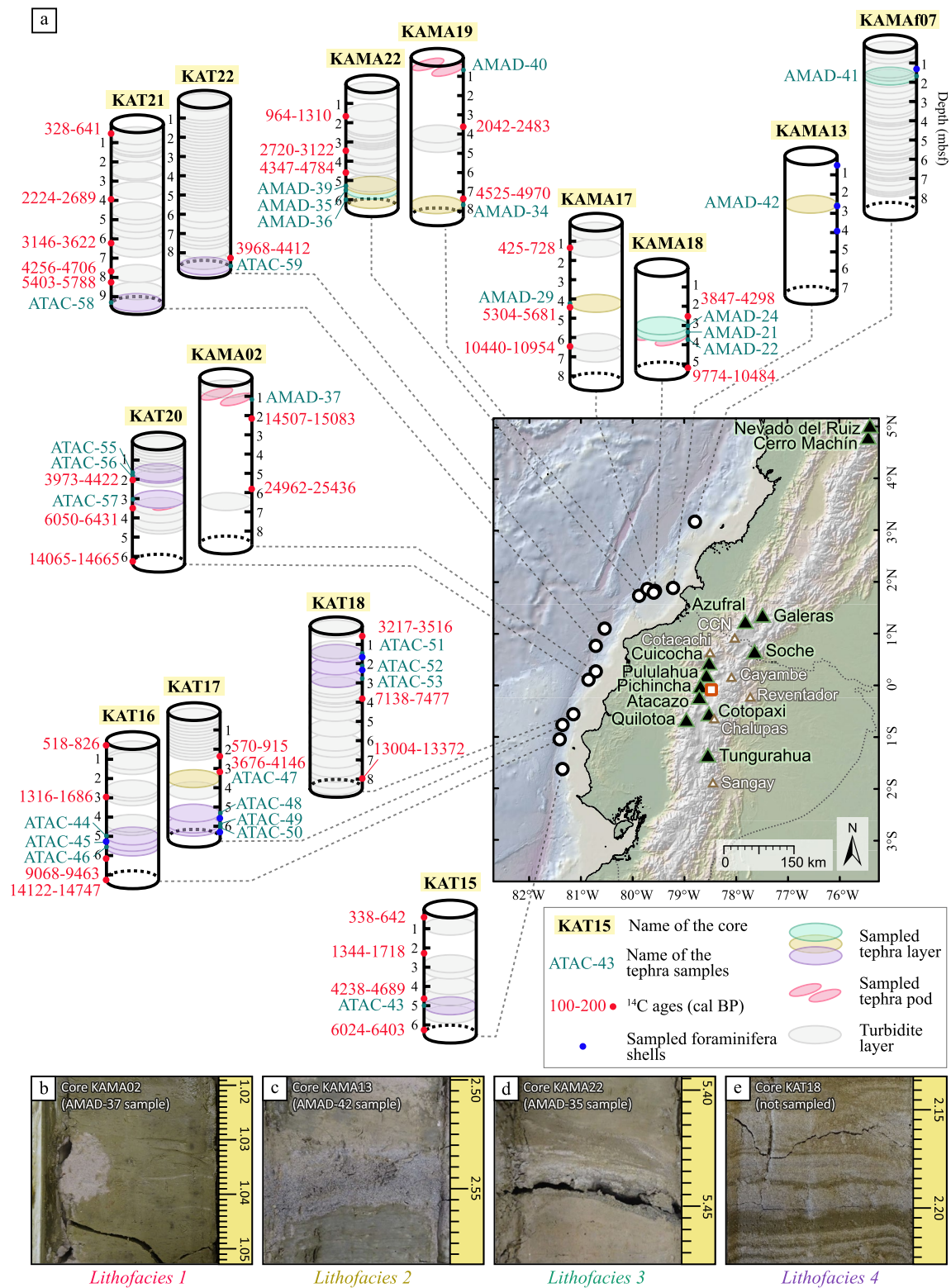


**Figure 2.** Tephra layers sampled in this study. (a) Synthetic diagrams of the sampled cores showing the location of marine sedimentary cores, the depth of available radiocarbon ages (data from Ratzov (2009) and Gonzalez (2018), detailed and calibrated in Data Set S1) performed on planktonic foraminifera given at 1-σ, sampled tephra layers (depth and thickness are given in Table 2) and turbidite sequences. Colors of sampled tephra layers are associated with their lithofacies, illustrated in Figures 2b–2e. Black and green triangles represent Ecuadorian and Colombian volcanoes that experienced at least one major eruption during the past 11 ka and whose eruptive history is summarized in the text. CCN: Chile-Cerro Negro. Red and white square: Quito. (b–e) Photograph of tephra layers of different structures (tephra pod, distinct and undistorted bed, laminated layer, and turbidite layers, respectively). The depth of the sections is indicated in m from the core top.

high  $^{143}\text{Nd}/^{144}\text{Nd}$  ratios ( $\sim 0.7040$  and  $\sim 0.5129$ , respectively) in the southern part of the Eastern Cordillera, and a high  $^{87}\text{Sr}/^{86}\text{Sr}$  and low  $^{143}\text{Nd}/^{144}\text{Nd}$  ratios ( $> 0.7043$  and  $< 0.5128$ , respectively; Ancellin et al., 2017) in the Western Cordillera. Such geochemical trends are interpreted as an increase of the crustal contamination in the southern part of the arc, as well as a decrease of the aqueous fluid/siliceous slab melt ratio away from  $0.5^\circ\text{S}$ .

Few isotopic data are available for the Colombian arc, except for Galeras (James & Murcia, 1984), Nevado del Ruiz (James & Murcia, 1984; Melson et al., 1990), Cerro Machín (Errázuriz-Henao et al., 2019; Laeger et al., 2013), Combia (Jaramillo et al., 2019), and Nevado del Santa Isabel (Errázuriz-Henao et al., 2019) volcanoes. Cerro Machín is distinguished by a significantly higher  $^{87}\text{Sr}/^{86}\text{Sr}$  ratio ( $\sim 0.7050$ ) and Galeras by a higher  $^{206}\text{Pb}/^{204}\text{Pb}$  ratio ( $\sim 19.2$ ), whereas other volcanoes are in the same data range as Ecuadorian volcanoes.

### 3. Materials and Methods

#### 3.1. Sampling

Coring sites of *Amadeus* (2005) and *Atacames* (2012) campaigns (KAMA- and KAT-cores, respectively) used in this study are located between  $1.7^\circ\text{S}$  and  $3.2^\circ\text{N}$  along the Ecuadorian and Colombian trench and forearc basins (Figure 1b). Core sections are stored at Géoazur and Géosciences Rennes Laboratories (France). We sampled 28 tephra layers from 14 marine cores (Figures 1 and 2) identified using both magnetic susceptibility data and visual description of sedimentary beds (Gonzalez, 2018; Ratzov, 2009). The precise location of coring sites, stratigraphic position and description of each sample is given in Table 2. Clayey material was removed by washing and manually sieving tephra samples at  $50\ \mu\text{m}$ . Samples were then rinsed with deionized water. As the morphology and geochemistry of glass shards constitute fingerprints of each volcano (e.g., Lowe, 2011), it is essential to define the chemical and mineralogical composition of tephra layers to accurately identify their source. Seven additional  $^{14}\text{C}$  ages (blue points in Figure 2a) were performed on *Neogloboquadrina Dutertrei* and *Neogloboquadrina Pachyderma* planktonic foraminifera from hemipelagic beds at DirectAMS, Bothell, Washington (USA). They refine the age constraints of tephra layers based on  $^{14}\text{C}$  AMS ages (red points in Figure 2a) performed at LMC14 LAB, Saclay (France), and provided by Ratzov (2009) and Gonzalez (2018). Age calibrations are detailed in Data Set S1.

#### 3.2. Scanning Electron Microscope

The size and morphology of glass shards, as well as any mineral inclusions, were assessed by scanning electron microscopy (SEM) at the Université Côte d'Azur (Nice, France). SEM observations and energy dispersive X-ray spectroscopy (EDX) analyses were carried out with a Tescan Vega3 XMU SEM (Tescan France, Fuveau, France) equipped with an Oxford X-MaxN 50 EDX detector (Oxford Instruments, Abingdon, UK) at accelerating voltages of 10 kV (imaging) and 20 kV (EDX). EDX spectra were processed with the Aztec software (version 3.2, Oxford Instruments). Samples were mounted on a SEM stub and carbon-coated prior to observations. SEM micrographs are given in Data Set S2 and EDX data in Data Set S3.

#### 3.3. Major and Trace Element Analyses

Chemical analysis of tephra is challenged by the small size of the glass shards ( $\sim 50\ \mu\text{m}$ ), which sometimes contain mineral inclusion that could bias the measurement. We therefore performed several techniques to determine the major and trace element content of our tephra layer samples. Electron Microprobe and Laser Ablation Inductively Coupled Plasma Mass Spectrometry (LA-ICP-MS) have been applied on single glass shards. Cleaned samples were sieved at 100 or 160  $\mu\text{m}$  depending on the average size of glass shards, and largest shards were individually selected and mounted on epoxy resin beads before polishing. Major element measurements were performed on CAMECA SXFive-TACTIS electron microprobe at the Laboratoire Magmas et Volcans (Clermont-Ferrand, France). Beam conditions were adjusted in order to minimize sodium loss during acquisition. Operating conditions were 15 kV accelerating voltage, 4 nA beam current and a 10  $\mu\text{m}$  defocused beam. Between 4 and 9 oxide analyses whose sum is  $> 95\%$  have been performed on different glass shards for each sample. Individual analyses were normalized to 100 wt.%, and averaged according to their geochemical similarity (i.e.,  $< 2.5\%$  variability for  $\text{SiO}_2$ ). Relative uncertainties are  $\sim 0.5\%$  for  $\text{SiO}_2$ , 1% for  $\text{K}_2\text{O}$  and  $\text{Al}_2\text{O}_3$ ,  $\sim 3\%$  for  $\text{CaO}$  and  $\text{Na}_2\text{O}$ , 5% for  $\text{FeO}$ ,  $\sim 10\%$  for  $\text{MgO}$ ,  $\sim 30\%$  for  $\text{TiO}_2$ , and  $\sim 130\%$  for  $\text{MnO}$  and  $\text{P}_2\text{O}_5$ . Trace elements measurements were performed

**Table 2**  
*Location and Composition of Sedimentary Cores, and Depth of Sampled Tephra Layers*

Core	Coring site coordinates	Water depth	Location of the coring site and description of the core	Tephra layer depth (mbsf)	Sample name	Lithofacies
KAMA02	N 00°12'965 W 80°39'430	1,315 m	Middle slope sediment: south of the Atacames seamounts. Homogeneous silty clay sedimentation, hemipelagic mud with some bioturbation	1.06–1.11	AMAD-37	1 (tephra pod)
KAMA07	N 03°11'3.43 W 78°48'55.6	2,903 m	Piggyback basin overlying the Colombian accretionary prism. Sections are composed of several bioturbated turbidite beds from 1.5 mbsf	1.76–1.78	AMAD-41	3 (laminated ashfall deposit with sharp lower and upper contact)
KAMA13	N 01°54'.063  W 79°12'.912	714 m	Tumaco forearc basin: small perched basin, upper slope of Tumaco basin, protected from major terrigenous inputs	2.54–2.57	AMAD-42	2 (primary ashfall deposit with sharp upper and lower contacts)
KAMA17	N 01°43'.08 W 79°27'.8	865 m	Manglares forearc basin: south of Manglares deep fault. Silty clay sedimentation with some coarse turbiditic material	4.27–4.34	AMAD-29	2 (primary ashfall deposit with sharp upper and lower contacts)
KAMA18	N 01°43'37.82  W 79°27'29.71	864 m	Manglares forearc basin: north of Manglares deep fault, protected from major terrigenous inputs. Homogeneous silty clay sedimentation	3.06–3.07	AMAD-24	3 (ashfall deposit with sharp lower contact and diffuse upper contact)
				3.16–3.17	AMAD-21	3 (ashfall deposit with sharp lower contact and diffuse upper contact)
KAMA19	N 01°45'13.24 W 79°35'3.52	737 m	Manglares forearc basin: depocenter along the Ancon fault. Homogeneous silty clay sedimentation with many bioturbations and two small turbidites	3.54–3.55	AMAD-22	1 (tephra pod)
				0.48–0.49	AMAD-40	1 (tephra pod)
KAMA22	N 01°38'34.49  W 70°45'53.62	1,432 m	Tumaco forearc basin: depocenter along the Ancon fault and the Esmeraldas Canyon, isolated from terrestrial inputs. Hemipelagites interbedded with hemipelagic turbidites that come from the local failure of the hemipelagic cover	7.65–7.68	AMAD-34	2 (primary ashfall deposit with sharp upper and lower contacts)
				5.34–5.35	AMAD-39	2 (primary ashfall deposit with sharp upper and lower contacts)
KAMA22	N 01°38'34.49  W 70°45'53.62	1,432 m	Tumaco forearc basin: depocenter along the Ancon fault and the Esmeraldas Canyon, isolated from terrestrial inputs. Hemipelagites interbedded with hemipelagic turbidites that come from the local failure of the hemipelagic cover	5.43–5.45	AMAD-35	3 (ashfall deposit with sharp lower contact and diffuse upper contact)
				5.96–5.98	AMAD-36	2 (primary ashfall deposit with sharp upper and lower contacts)
KAT15	S 01°40'49.44 W 81°16'50.18	2,324 m	Slope basin in the middle slope, ~50 km north of the Santa Elena Canyon. Heterogeneous silty to sandy sedimentation with several turbidite beds	5.06–5.07	ATAC-43	4 (tephra layer within turbidite beds)

**Table 2**  
*Continued*

Core	Coring site coordinates	Water depth	Location of the coring site and description of the core	Tephra layer depth (mbsf)	Sample name	Lithofacies
KAT16	S 01°06'28.86 W 81°20'59.88	3,238 m	Trench: west of the Manta Peninsula. Silty to sandy sedimentation with several thick turbidite beds	5.04–5.05	ATAC-44	4 (tephra layer within turbidite beds)
				5.42–5.43	ATAC-45	4 (tephra layer within turbidite beds)
				5.78–5.79	ATAC-46	4 (tephra layer within turbidite beds)
KAT17	S 00°49'31.80 W 81°17'19.80	3,324 m	Trench: westward of Manta City. Top sections are composed of homogeneous clay without tephra or bioturbation, deeper sections are composed of turbidite beds with several tephra layers	3.61–3.62	ATAC-47	2 (primary ashfall deposit with sharp upper and lower contacts)
				5.19–5.20	ATAC-48	4 (tephra layer within turbidite beds)
				5.95–5.96	ATAC-49	4 (tephra layer within turbidite beds)
KAT18	S 00°37'11.76 W 81°04'50.34	1,606 m	Middle slope basin. Heterogeneous sedimentation with several tephra layers in sections I to III interbedded with graded layers enriched in foraminifera, and highly bioturbated clay layers in deeper sections	1.56–1.57	ATAC-51	4 (tephra layer within turbidite beds)
				2.07–2.08	ATAC-52	4 (tephra layer within turbidite beds)
				2.86–2.87	ATAC-53	4 (tephra layer within turbidite beds)
KAT20	N 00°00'41.76 W 80°49'30.36	1,918 m	Middle slope basin: basin: ~20 km south of the Atacames seamounts. Homogeneous silt to clay sedimentation with lots of bioturbation and some turbidite beds separated by hemipelagic layers	1.83–1.84	ATAC-55	4 (reworked tephra layer within turbidite beds)
				1.89–1.90	ATAC-56	4 (reworked tephra layer within turbidite beds)
				2.93–2.94	ATAC-57	4 (tephra layer within turbidite beds)
KAT21	N 00°39'49.14 W 80°38'55.32	3,802 m	Trench sub-basin: foot of the lower slope in front of Punta Galera. Mainly hemipelagic sedimentation with several bioturbated turbidite layers	9.23–9.24	ATAC-58	4 (tephra layer within turbidite beds)
KAT22	N 00°59'41.16 W 80°28'29.46	3,962 m	Trench sub-basin: foot of the lower slope in front of Punta Galera. Homogeneous clayey sedimentation with several turbidite beds without bioturbation	8.82–8.84	ATAC-59	4 (tephra layer within turbidite beds)

*Note.* The depth of the tephra layers is indicated in meters below sea floor (mbsf) from the core top. Lithofacies are described in Section 4.1.

on the same glass shards on an Element XR HR-ICP-MS spectrometer coupled with a 193 nm Resonetics Excimer laser ablation at the Laboratoire Magmas et Volcans (Clermont-Ferrand, France). Beam diameter was set between 12 and 20  $\mu\text{m}$ , with a 1 Hz repetition rate and 2.8 J/cm<sup>2</sup> fluency. GSE USGS standard was used as primary standard and 27Al as internal standard. GSD and BCR-2G were used as secondary standards. Relative uncertainties are ~5% for Na, Al, Rb, Sr, Nb, Ba, La, and Th, ~12% for Ca, Mn, Y, and Zr, and 50%–75% for Li, Ni, Cu, and Yb. Inductively Coupled Plasma—Atomic Emission Spectrometry (ICP-AES) analyses were also performed on whole-rock (bulk tephra samples) to determine trace elements. Cleaned samples were leached by 5% HCl solution during 10 min to dissolve foraminifera shells and calcareous fossils, then rinsed and centrifuged twice (3,000 rpm for 10 min) with deionized water, rinsed with ethanol, and dried at 50°C. This procedure was repeated until the

samples no longer showed any apparent carbonates. A magnetic separator was then used to remove the possible xenoliths. Agate-crushed powders of bulk glass shards with scarce non-magnetic phenocrysts such as plagioclase or quartz were measured at the Laboratoire Géosciences Océan of the Université de Bretagne Occidentale (Brest, France), following the procedure detailed in Cotten et al. (1995). Relative uncertainties are  $\leq 5\%$  for most trace elements. Minor and trace element contents are presented in Data Set S3. Ni, Y, and Yb contents measured by LA-ICP-MS on single glass shards were often under the detection limit. As ICP-AES measurements performed on bulk tephra samples are in agreement with the maximum contents measured by LA-ICP-MS for these three elements, we used ICP-AES for the latter and elements that were not analyzed by LA-ICP-MS (indicated in yellow in Data Set S3).

### 3.4. Sr-Pb Isotope Analyses

Samples of 17 representative tephra layers were prepared following the same procedure as ICP-AES analyses, and powders of bulk glass shards with scarce non-magnetic phenocrysts such as plagioclase or quartz were dissolved following the procedure detailed in Ancellin et al. (2017). For Sr and Pb isotopes, between 100 and 200 mg of sample were weighed in a 15 mL Savillex. Prior digestion, samples were leached in a solution of HCl 6N on a hot plate at 50°C during 1 hr. After leaching, samples were rinsed several times with ultrapure water. Then, samples were digested using a solution of 14 M HNO<sub>3</sub> and 28 M HF (1 and 4 mL, respectively). The whole mixture was heated on a hot plate at 115°C for 24–48 hr, evaporated to dryness, dissolved in 6 M HCl, and heated again for 24 hr. After complete dissolution and subsequent evaporation, the residue was diluted in 2 ml of 2 M HNO<sub>3</sub>. Sr and Pb were separated using the Sr spec resin (Pin & Gannoun, 2017).

Sr isotope compositions were measured at Laboratoire Magmas et Volcans (Clermont-Ferrand, France). The Sr cuts were loaded onto Re filaments and analyzed by TIMS Triton Plus (Thermo electron) in static multicollection. The <sup>87</sup>Sr/<sup>86</sup>Sr ratios were normalized to an <sup>86</sup>Sr/<sup>88</sup>Sr ratio of 0.1194. Repeated analysis of the NBS 987 standard yielded an average of  $0.710255 \pm 0.000017$ . We used international standards (AGV-2, BHVO-2, RGM-1, and BCR-2) to test the reproducibility of our method. Values obtained for AGV-2 (<sup>87</sup>Sr/<sup>86</sup>Sr =  $0.703978 \pm 11$ ;  $n = 2$ ), BHVO-2 (<sup>87</sup>Sr/<sup>86</sup>Sr =  $0.703469 \pm 11$ ;  $n = 10$ ), RGM-1 (<sup>87</sup>Sr/<sup>86</sup>Sr =  $0.704192 \pm 10$ ;  $n = 2$ ), and BCR-2 (<sup>87</sup>Sr/<sup>86</sup>Sr =  $0.705009 \pm 6$ ;  $n = 1$ ), are in agreement with the international reference values (Jochum et al., 2005).

Pb isotope ratios were measured on an MC-ICP-MS Neptune plus (Thermo electron) at Laboratoire Magmas et Volcans (Clermont-Ferrand, France). The procedural blanks (<100 pg) were negligible compared to the amount of lead purified (>200 ng). Instrumental mass fractionation was corrected using Tl-doping (White et al., 2000). The measured ratios were subsequently normalized by linear interpolation using the <sup>206</sup>Pb/<sup>204</sup>Pb, <sup>207</sup>Pb/<sup>204</sup>Pb, and <sup>208</sup>Pb/<sup>204</sup>Pb values of Galer and Abouchami (1998) for NBS981 (16.9405, 15.4963, and 36.7219, respectively). We used international standards (AGV-2, RGM-1, and BCR-2) to test the reproducibility of our method. Values obtained for AGV-2 (<sup>206</sup>Pb/<sup>204</sup>Pb =  $18.872 \pm 3$ ; <sup>207</sup>Pb/<sup>204</sup>Pb =  $15.618 \pm 2$ ; and <sup>208</sup>Pb/<sup>204</sup>Pb =  $38.549 \pm 5$ ;  $n = 11$ ), RGM-1 (<sup>206</sup>Pb/<sup>204</sup>Pb =  $19.005 \pm 1$ ; <sup>207</sup>Pb/<sup>204</sup>Pb =  $15.635 \pm 2$ ; and <sup>208</sup>Pb/<sup>204</sup>Pb =  $38.710 \pm 5$ ;  $n = 3$ ), and BCR-2 (<sup>206</sup>Pb/<sup>204</sup>Pb =  $18.758 \pm 1$ ; <sup>207</sup>Pb/<sup>204</sup>Pb =  $15.624 \pm 2$ ; and <sup>208</sup>Pb/<sup>204</sup>Pb =  $38.745 \pm 5$ ;  $n = 3$ ), are in agreement with the international reference values (Jochum et al., 2005).

Results of Sr and Pb isotope ratios are presented in Data Set S3.

## 4. Results

### 4.1. Lithofacies of Tephra Layers

The depth and thickness of sampled tephra layers are given on Table 2. Based on the sedimentary facies and structures of tephra layers, we identified four lithofacies.

#### 4.1.1. Lithofacies 1

This facies corresponds to fine to coarse volcanic glass shards with crystals and scarce lithics forming a sub-spherical pod, a few centimeters in diameter, in sharp contact with silty-clay marine sediments (e.g., Figure 2b). Such facies is found in three cores (samples AMAD-22, -37, and -40 in KAMA18, KAMA02, and KAMA19 cores). AMAD-22 pod is overlaid by a lithofacies 3 deposit that contains similar other glass shards, whereas AMAD-37 and AMAD-40 pods are independent of any other tephra deposits within their respective sedimentary cores.



#### 4.1.2. Lithofacies 2

This facies consists of a layer with a high abundance of pinkish to light gray, angular to sub-angular glass shards with sharpened edges, crystals and scarce lithics. This layer presents a sharp non-erosive basal contact and a sharp upper contact with silty-clay marine sediments (e.g., Figure 2c). It contains few carbonate shells and foraminifera, and no evidence of bioturbation. The median grain size does not exceed 65  $\mu\text{m}$ , and the layer presents a normal grading. This facies depicts AMAD-42 (KAMA13 core), AMAD-29 (KAMA17 core), AMAD-34 (KAMA19 core), ATAC-47 (KAT17 core), and AMAD-36 and 39 (KAMA22 core) tephra layers.

#### 4.1.3. Lithofacies 3

The basal part of this facies is similar to lithofacies 2, with a normal grading, and a high abundance of angular to sub-angular glass shards with sharpened edges and minerals. In some cases, it also exhibits a sharp truncating lower contact with silty-clay marine sediments. The upper part of the tephra layer presents thin parallel planar laminations, and a diffuse, gradational and/or bioturbated upper contact (e.g., Figure 2d). Glass shards show a variation in color from ochre to light gray, and their size ranges from fine to coarse. This facies is common and observed in AMAD-41 (KAMAf07 core), AMAD-21 and 24 (KAMA18 core), AMAD-35 (KAMA22 core), and ATAC-55 and 56 (KAT20 core) tephra layers.

#### 4.1.4. Lithofacies 4

It is composed of overlaying thin laminated layers with sharp erosional bases suggesting deposition by high-velocity gravity flows. Tephra layers are enriched in fine, light gray or two-tones glass shards with crystals and lithics, and thin normally graded layers of marine sediments often enriched in carbonate shells and foraminifera. The thickness of layers varies from few millimeters to several tens of centimeters (Figure 2e). This facies is mainly observed in cores located in the southern part of our study site (KAT15 to 20; Figure 2a), in which numerous turbidite beds have been described (Gonzalez, 2018), and corresponds to all tephra layers present in these cores, except ATAC-47 that is associated with lithofacies 2.

### 4.2. Morphology of Glass Shards and Mineralogy of Tephra Layers

The mineralogy and morphology of sampled tephra layers is detailed in Figure 3a. The color of tephra layers varies from light to dark gray, but it can be ochre due to the presence of sulfur (AMAD-21 sample).

The morphology of glass shards is heterogeneous, and varies between bubble-wall (massive shard with thick vesicle wall, Figure 3b), pumiceous (highly vesicular and indicating a large proportion of exsolved volatiles in the erupting magma, Figure 3c), blocky (vesicle poor, Figure 3d), cusped (remnant bubble walls of large vesicles from coarse pumices fragmented in the vent or the plume, Figure 3c) and tabular (highly stretched vesicles, Figure 3b) shapes. Vesicles are generally small (<20  $\mu\text{m}$  and rarely over 40  $\mu\text{m}$ ), round to elliptical, and generally elongated in shape. Samples AMAD-41, ATAC-55, and ATAC-56 (cores KAMAf07 and KAT20) are distinctive because they are almost exclusively composed of blocky-shaped shards, whereas ATAC-45 and ATAC-53 samples (cores KAT16 and KAT18, respectively) are mainly made up of bubble-wall-shaped shards, and ATAC-43 (core KAT15) contains the highest proportion of cusped shards.

Tephra layers are glass shard rich (~90%) and fine (<150  $\mu\text{m}$ ), and poor in lithic fragments, except for ATAC-55 and ATAC-56 samples, which contain ~40% glass shards and ~50% lithics. All samples contain abundant plagioclase (60–90  $\mu\text{m}$ ) and amphibole (60–120  $\mu\text{m}$ , Figure 3f) crystals, and most of them contain Fe-Ti oxides, generally as inclusion or coated with glass shards. Some samples also contain larger biotite crystals (80–150  $\mu\text{m}$ , Figures 3a and 3e), as well as quartz (60–90  $\mu\text{m}$ ; AMAD-37-39 and ATAC-48-53 samples). The oxide content of single crystals determined by SEM-EDX analyses is given in Text S1 in Supporting Information S2. Glass shards occasionally bear microlites of plagioclase, amphibole, apatite and zircon (Figure 3a), and present conchoidal fractured surfaces.

### 4.3. Geochemistry

Major element contents of each tephra layer determined using electron microprobe on single glass shards are given in Data Set S3 and  $\text{K}_2\text{O}$  versus silica contents are plotted in Figure 4a.

Marine tephra samples belong to the medium- and high-K calc-alkaline magmatic series, with  $\text{K}_2\text{O}$  contents ranging between 1.9 and 4.0 wt.%. All samples display a homogeneous rhyolitic composition with  $\text{SiO}_2$  contents

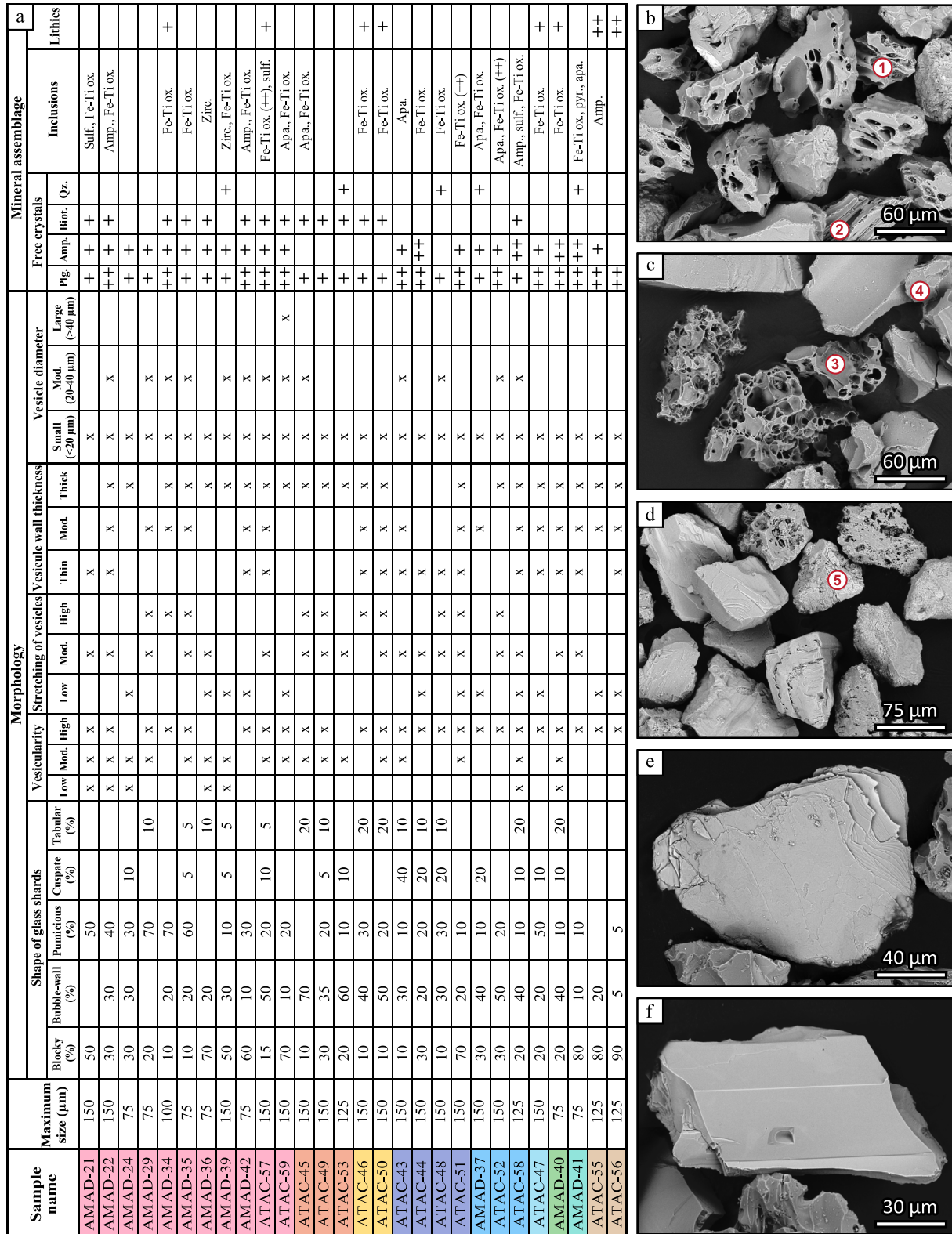
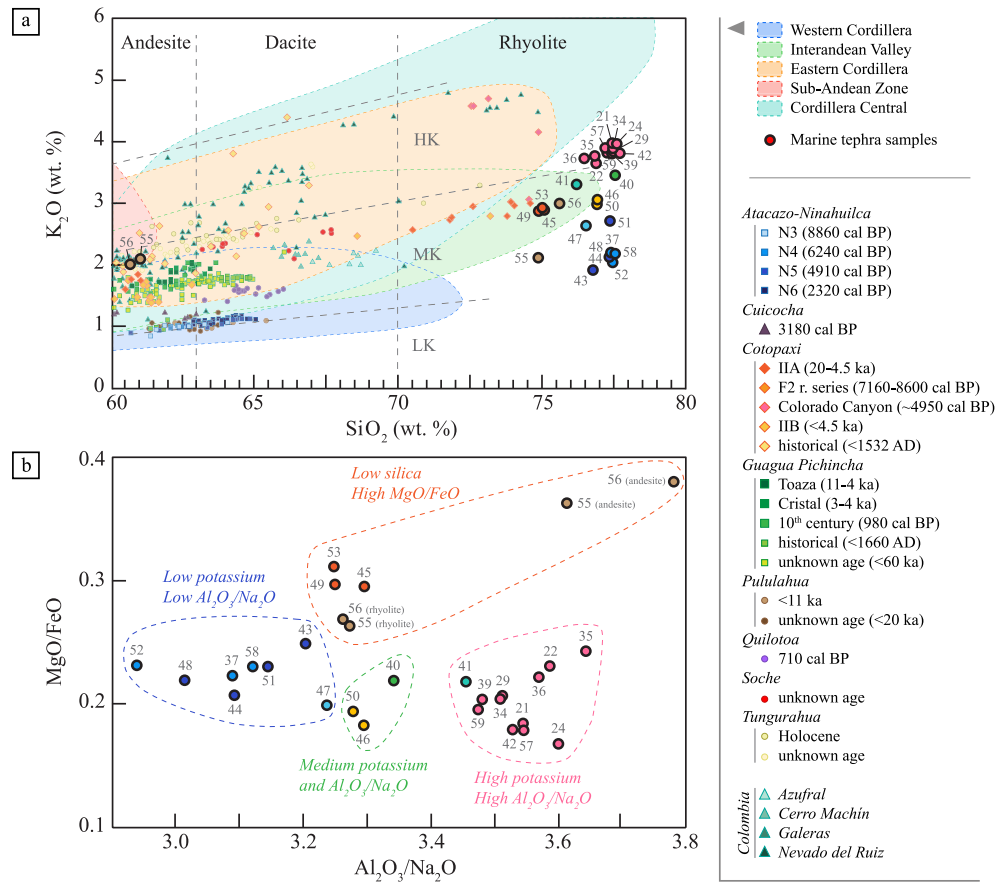
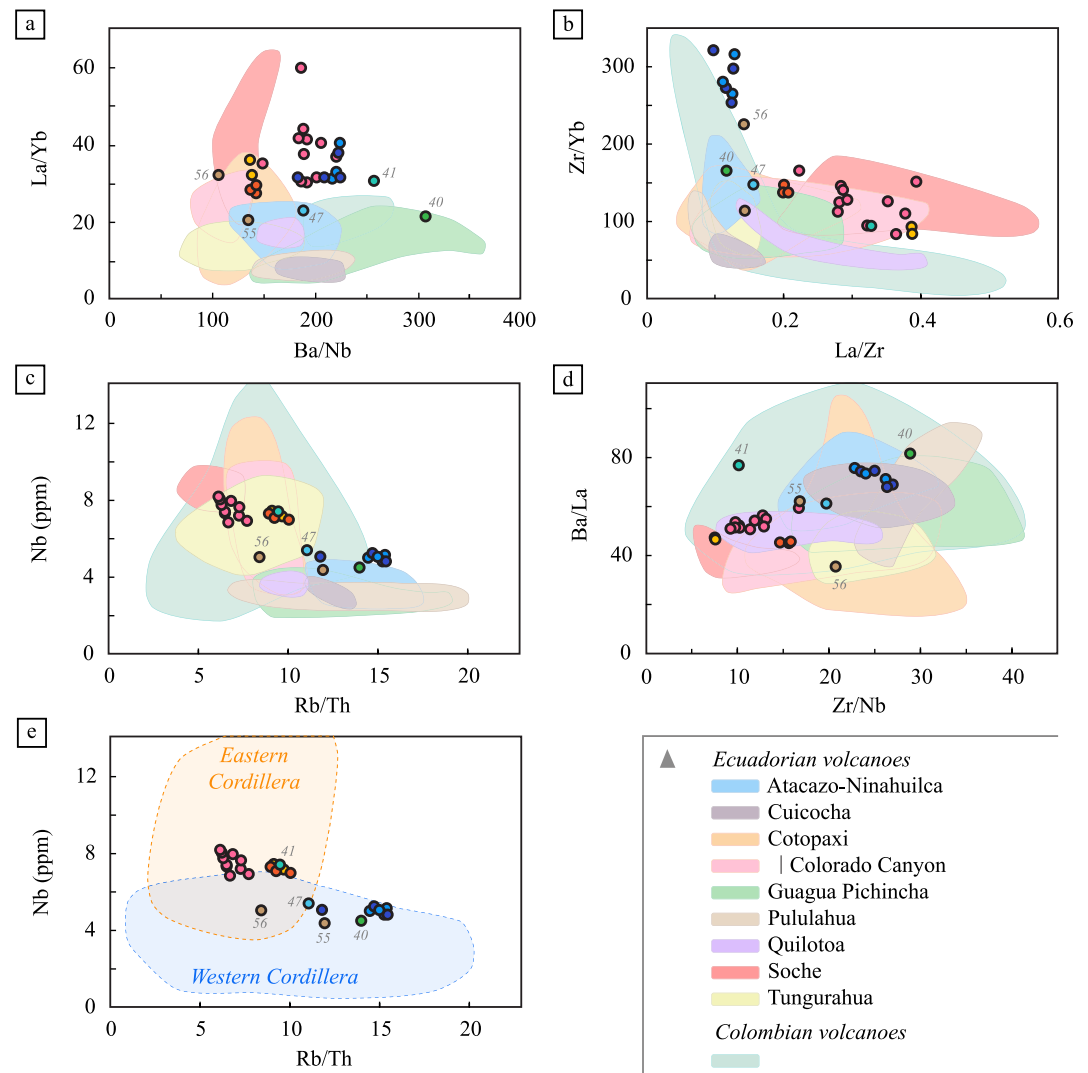


Figure 3.



**Figure 4.** Major element composition of marine tephra layers. (a) K<sub>2</sub>O versus SiO<sub>2</sub> diagram with composition fields of all data obtained for the Ecuadorian and Colombian arcs (Georoc database). Points with black contour: average of single glass shards measurements performed on studied marine tephra by Electron Microprobe (Data Set S3). Numbers: sample name (AMAD-xx or ATAC-xx). HK, MK, LK: high-, medium-, and low-K calc-alkaline series. Two points for ATAC-55 and ATAC-56 samples illustrate their heterogeneous composition, made up of a mixture between andesite and rhyolite glass shards. Small symbols correspond to analyses performed onland on major Holocene eruptions from Atacazo-Ninahuilca (whole rock on pumices and blocks from pyroclastic flow deposits, Hidalgo et al., 2008), Cuicocha (whole rock measurements, Schiano et al., 2010), Cotopaxi (whole rock on lava flows and pyroclastic fall deposits, Garrison et al. (2006, 2011); bulk tephra from the 2015 AD eruption measurements, Hidalgo et al. (2018); whole rock on scoria clasts from 1532 to 1768 AD eruptions and on tephra from the 1877 AD eruption, Saalfeld et al. (2019)), Pichincha (whole rock samples from Guagua Pichincha, Samaniego et al. (2010) and Schiano et al. (2010)), Pululahua (whole rock on lava flows, Bryant et al. (2006) and Chiaradia et al. (2009, 2014)), Quilotoa (whole rock on lava flows, Bryant et al. (2006) and Ancellin et al. (2017)), Tungurahua (whole rock measurements, Hall et al. (1999), Schiano et al. (2010), Samaniego et al. (2011), Myers et al. (2014), Bablon et al. (2018), Nauret et al. (2018), and Ancellin et al. (2017)), and Colombian volcanoes (whole-rock on undated scoria clasts, pumice and lavas for Azufral, Cerro Machín and Galeras volcanoes, Marriner and Millward (1984), Droux and Delaloye (1996), Calvache and Williams (1997), Laeger et al. (2013), Ancellin et al. (2017), and Errázuriz-Henao et al. (2019); single glass shard from the 1985 AD pyroclastic deposits, Calvache (1990), Vatin-Pérignon et al. (1990); and whole rock on scoria and pumices from the 1985 AD eruption, Gourgaud and Thouret (1990), Sigurdsson et al. (1990), and Melson et al. (1990), for Nevado del Ruiz volcano). (b) MgO/FeO versus Al<sub>2</sub>O<sub>3</sub>/Na<sub>2</sub>O diagram of marine tephra layers. Each point represents average of single shards measurements performed by Electron Microprobe (Data Set S3). Tephra layers with similar composition are represented by the same color, which is also used in the following figures.

**Figure 3.** Synthesis of the morphological and mineralogical characteristics of the tephra layers studied. (a) Table of the morphology and mineral assemblage of sampled tephra layers based on binocular magnifier observation, as well as scanning electron microscopy (SEM) and dispersive X-ray spectroscopy analyses. Descriptors based on Nelson et al. (1985) and Lowe (2011). Plg.: plagioclase, Amp.: amphibole, Biot.: biotite, ox.: oxide, Qz.: quartz, Pyr.: pyroxene, Sulf.: sulfur, Zirc.: zircon, Apa.: apatite. The color code of samples is the same one used in the following figures and represents their source discussed in the following sections. SEM images of all samples are available in Data Set S2. (b) SEM image of bubble-wall-shaped shards (1; ATAC-45 sample). The white part of the shard in the upper left corner of the image is a Fe-Ti oxide coating. Note a tabular shard in the lower right corner (2). (c) SEM image of pumiceous-shaped (3) and cuspsate (4) shards (ATAC-48 sample). (d) SEM image of blocky-shaped shards (5; ATAC-55 sample). (e) SEM image of a biotite crystal with a sheet structure (ATAC-57 sample). (f) SEM image of an amphibole crystal (AMAD-36 sample).



**Figure 5.** Trace element diagrams. (a–d) Comparison between the composition of glass shards of marine tephra layers (circles, same colors as in Figure 4) with onland products from Holocene major eruptions (same references as in Figure 4a). Each trace element content has been measured on single glass shard by LA-ICP-MS and averaged for each sample, except Yb contents that were measured on bulk glass shards by ICP-AES. The numbers refer to the name of the samples whose source is distinguished from the others, and is discussed in the text. (e) Comparison between the composition of glass shards of marine tephra layers and the composition fields obtained for all volcanoes from the Western and Eastern Cordilleras of Ecuador (blue- and orange-colored areas, respectively; georoc data).

higher than 74.8 wt.% (standard deviations are given in Data Set S3), except for samples ATAC-55 and ATAC-56 (core KAT20), which also present andesite glass shards, with  $\text{SiO}_2$  contents of  $\sim 62$  wt.%. This diagram reveals groups of tephra of similar composition, which are distinguished by their alkaline and silica contents (Figure 4a), but also by their  $\text{MgO/FeO}$  and  $\text{Al}_2\text{O}_3/\text{Na}_2\text{O}$  ratios (Figure 4b). Tephra with the highest  $\text{K}_2\text{O}$  contents present the highest  $\text{Al}_2\text{O}_3/\text{Na}_2\text{O}$  ratios ( $\sim 3.35$  to  $3.65$ ; pink, turquoise and light green points, Figure 4b), whereas tephra with the lowest  $\text{K}_2\text{O}$  contents present the lowest  $\text{Al}_2\text{O}_3/\text{Na}_2\text{O}$  ratios ( $\sim 2.95$  to  $3.3$ ; blue points, Figure 4b), and tephra with the lowest  $\text{SiO}_2$  contents present the highest  $\text{MgO/FeO}$  ratios ( $\sim 0.25$  to  $0.4$ ; orange and brown points, Figure 4b). These groups allow a first correlation of several of the tephra layers present in the cores.

This rough correlation can be refined by considering the trace element compositions of tephra layers. In particular, the group of tephra with the high  $\text{K}_2\text{O}$  contents and high  $\text{Al}_2\text{O}_3/\text{Na}_2\text{O}$  ratios presents enrichments in Nb, high La/Yb and La/Zr ratios, and low Zr/Yb, Rb/Th, and Zr/Nb ratios compared to other tephra layers (pink and turquoise points, Figures 5a–5d). Similarly, the group with the low  $\text{K}_2\text{O}$  contents and low  $\text{Al}_2\text{O}_3/\text{Na}_2\text{O}$  ratios present significantly higher Zr/Yb and Rb/Th ratios (blue points, Figures 5b and 5c), and the group with the low

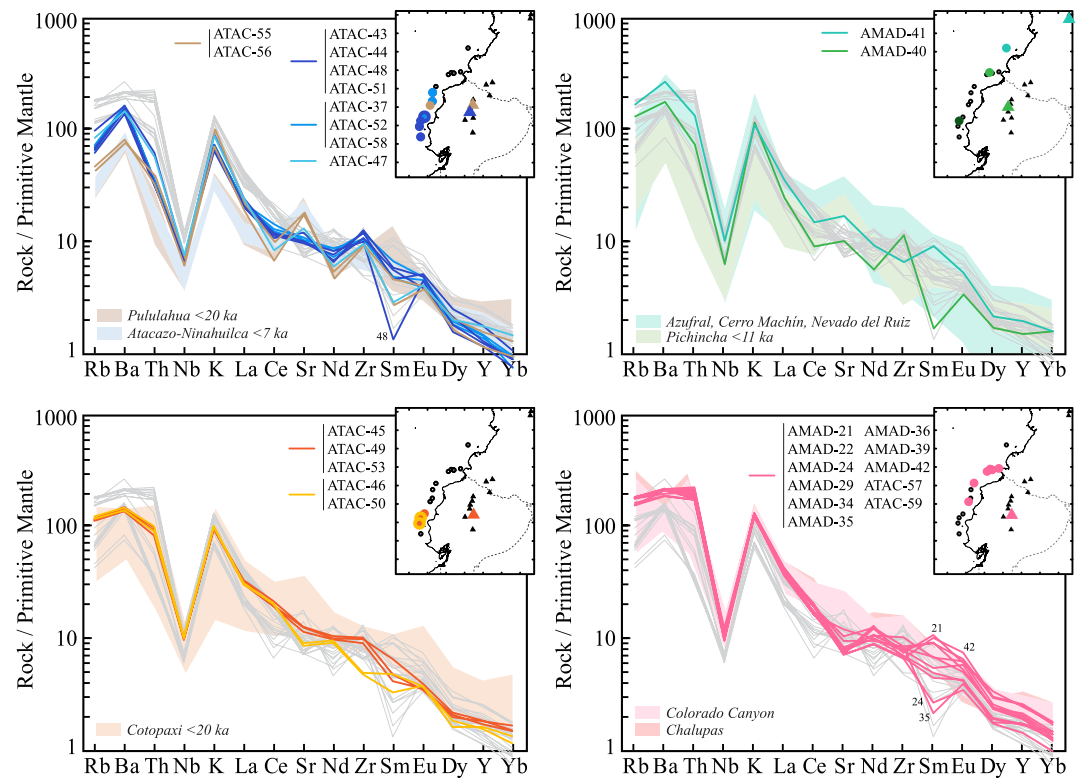


**Figure 6.** Incompatible elements normalized to primitive mantle spider diagram (Sun & McDonough, 1989). Colored domains represent the range of values obtained for the onland deposits of major recent eruptions (same references as Figure 3a; Chalupas data: single glass shards on distal marine tephra, Bablon, Quidelleur, Siani, et al. (2020)).

SiO<sub>2</sub> contents and high MgO/FeO ratios present the lowest Ba/Nb and Ba/La ratios (orange and brown points, Figures 5a and 5d). In addition, all tephra layers are enriched in most incompatible elements (e.g., Rb, Ba, Th, and K) and highly depleted in Nb (Figure 6), typical of subduction-related volcanic products. Consequently, they cannot originate from the Galápagos Islands (Figure 1).

Pb ratios are heterogeneous, ranging between 18.897 and 19.044, between 15.604 and 15.663, and between 38.637 and 38.876, for <sup>206</sup>Pb/<sup>204</sup>Pb, <sup>207</sup>Pb/<sup>204</sup>Pb, and <sup>208</sup>Pb/<sup>204</sup>Pb, respectively. <sup>87</sup>Sr/<sup>86</sup>Sr ratios vary between 0.7040 and 0.7045, except for AMAD-41 sample, whose ratio is significantly higher and reach 0.7049. Samples belonging to the group of tephra with the highest K<sub>2</sub>O contents have high <sup>206</sup>Pb/<sup>204</sup>Pb, <sup>207</sup>Pb/<sup>204</sup>Pb, and <sup>87</sup>Sr/<sup>86</sup>Sr ratios (pink points, Figures 7a and 7b). Lowest <sup>207</sup>Pb/<sup>204</sup>Pb and <sup>87</sup>Sr/<sup>86</sup>Sr ratios are found for AMAD-40 and ATAC-47 samples (green and light blue points, Figures 7a and 7b), and lowest <sup>206</sup>Pb/<sup>204</sup>Pb ratio matches the ATAC-55 and ATAC-56 samples (brown points, Figure 7a).

## 5. Discussion

### 5.1. Deposition Processes of Marine Tephra Layers on the Continental Margin

The potential of the volcanoclastic layers identified in the cores to reliably record major eruptions and to constitute chronostratigraphic markers rely on their primary versus reworked nature, especially at sites where turbidite beds are evidenced (Figure 2a). We interpret the deposition processes of the four different lithofacies as follows.

#### 5.1.1. Lithofacies 1: Bioturbated Primary Tephra Fallouts

Marine tephra layers thinner than a few centimeters can be bioturbated by burrowing fauna and become *tephra pods* some weeks to years after the deposition (Hopkins et al., 2020; Wetzel, 2009). Such phenomena probably occurred with former AMAD-22, AMAD-37, and AMAD-40 tephra layers, which presently appears as relics in KAMA18, KAMA02, and KAMA19 cores, respectively (lithofacies 1; e.g., Figure 2b). Depending on the type of benthic fauna, the pods could be either burrows infilling above or closely below the original deposit, or a

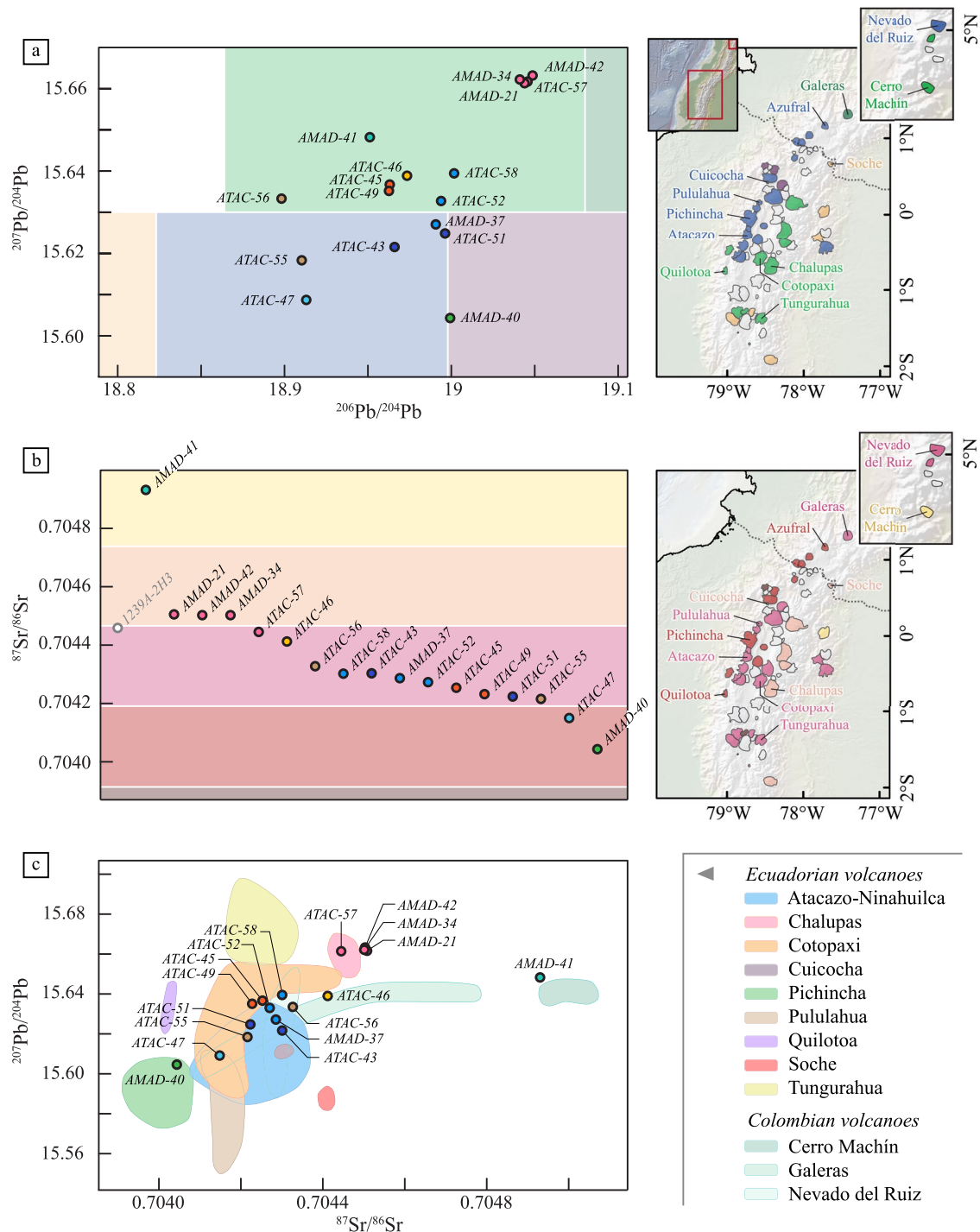


**Figure 7.** Comparison of isotopic data obtained on marine tephra and on onland proximal products. (a)  $^{207}\text{Pb}/^{204}\text{Pb}$  versus  $^{206}\text{Pb}/^{204}\text{Pb}$  diagram showing results obtained for marine tephra layers (circles with the same color as in Figures 4 and 5). The map on the right indicates the average values published for the Ecuadorian (Ancellin et al., 2017 and references therein; Chiaradia et al., 2020) and Colombian (Chiaradia et al., 2020; Errázuriz-Henao et al., 2019; James & Murcia, 1984; Jaramillo et al., 2019; Laeger et al., 2013; Melson et al., 1990) volcanoes, and associated colors are reported on graphics on the left as composition fields (modified from Ancellin et al. (2017)). (b)  $^{87}\text{Sr}/^{86}\text{Sr}$  results obtained for marine tephra layers presented from the largest to the smallest ratio. Colored fields correspond to value ranges obtained at the arc scale, as described in Figure 5b. 1239A-2H3 (white and gray point) is a control sample of a tephra layer collected in the ODP 1239 core (located 100 km west of KAT18 coring site, Figure 1a) and correlated with the 215 ka Chalupas ignimbrite (Bablon, Quidelleur, Siani, et al., 2020). Both Pb and Sr isotope ratio agree with those of onland deposits, showing that measurements performed on marine tephra are not biased by sea water or shells. (c)  $^{207}\text{Pb}/^{204}\text{Pb}$  versus  $^{87}\text{Sr}/^{86}\text{Sr}$  diagram with the composition range of volcanoes that experienced at least one major eruption during the Holocene (same references as Figure 7a).

discontinuous original deposit. As they seem independent of any other tephra deposit, they can represent burrows emplaced below the original primary deposit, which has been subsequently entirely redeposited or eroded, or correspond to a discontinuous original deposit (Hopkins et al., 2020). Their thickness and stratigraphic position should therefore be considered with caution.

### 5.1.2. Lithofacies 2 and 3: Primary Tephra Fallouts

Tephra layers characterized by a high content of glass shards (lithofacies 2; Figure 2c), or a gradation from an ash-rich layer into normal background sedimentation (lithofacies 3; Figure 2d), correspond to *subaerial ashfall* and later marine settling on the sea floor after each major volcanic event in the Cordillera.

The tephra deposits of lithofacies 2 occur in the Manglares basin and within small isolated basins no deeper than 500 m water depth (Figure 1b). After reaching the ocean surface, settling of tephra to these water depths is expected within a couple of days to a couple of months depending on the size of particles (Carey, 1997). A primary deposition by simple settling is compatible with the normal grading of the lithofacies 2 deposits. However, the settling of material through the water column is slower than in subaerial conditions, causing accumulation then overloading of tephra particles onto the water surface. This overloading creates density instabilities in the tephra layer, leading to the formation of descending plumes of material termed “diffuse vertical gravity current” (Carey, 1997; Manville & Wilson, 2004). Such a process accounts for settling velocities up to 10 times faster than calculated by the Stokes law for individual grains (Hopkins et al., 2020; Jacobs et al., 2015), and the arrival to the seafloor of a turbulent flow comparable to a turbidity current with a normal grading and sedimentary structures (planar and/or oblique laminations) as observed in the Bouma Sequence (Bouma, 1962), a *turbidite-like deposit, can be emplaced*. Such pattern is visible within lithofacies 3 (Figure 2d). Thin parallel laminations may also correspond to the late-stage fallout of the plume's fine-grained fraction (Sacchi et al., 2005). As stated by Manville and Wilson (2004), the distinction between a primary fall deposit and remobilized turbidites (see next section) may be complicated. Based on SEM images of both sharpened edges (Figures 3b and 3c) and low ruggedness (ratio of convex perimeter to total perimeter) of glass shards, we infer that the particles suffered limited transport within submarine turbidity currents as proposed by Gudmundsdóttir et al. (2011) offshore Iceland. Tephra deposits of both lithofacies 2 and 3 (i.e., the nine green and yellow layers, Figure 2a) could therefore be used as reliable stratigraphic markers.

### 5.1.3. Lithofacies 4: Tephra Fallouts Remobilized by Turbidity Currents

Lithofacies 4 (Figure 2d) is systematically encountered within turbidites, and therefore corresponds to secondary, reworked and redeposited tephra layers (Abbott et al., 2018; Freundt et al., 2021; Hopkins et al., 2020). However, the ruggedness and homogenous composition of glass shards suggest a potential (although limited) transport, and evidences a reworking/remobilization of a single original tephra layer for the deposition of each turbidite, except for ATAC-55 and ATAC-56 layers as discussed below. As compared to tephra layers retrieved offshore New-Zealand (e.g., Hopkins et al., 2020), these *volcaniclastic turbidites* suggest a relatively short-term storage on the shelf or margin slope before reworking. Given the frequency of earthquake-triggered turbidites in the studied area (Gonzalez, 2018; Migeon et al., 2017; Ratzov et al., 2010), the time span between deposition of the primary tephra and the one of the volcaniclastic turbidite should not exceed a couple of decades to centuries, and stand within the 1- $\sigma$  error bars of the calibrated  $^{14}\text{C}$  ages. We therefore consider that the stratigraphic position of these layers (i.e., the 15 purple layers, Figure 2a) in the cores and their age constraints remain robust. An exception to this assumption stands for tephra layers ATAC-55 and ATAC-56 (core KAT20) retrieved in a margin slope basin offshore central Ecuador (Figures 1b and 2a). They both present blocky-shaped glass shards of andesitic and rhyolitic composition (Figure 4a), and parallel laminations without hemipelagic deposits (Gonzalez, 2018). We interpret them as part of an *amalgamated turbidite*, which reflects the almost synchronous triggering of multiple slope failures during an earthquake (Goldfinger et al., 2007; Nakajima & Kanai, 2000; Van Daele et al., 2017). Both deposits therefore involve the reworking of numerous tephra layers, and their stratigraphic position is not made clear.

## 5.2. Correlation of Tephra Layers Between Coring Sites

Five groups of tephra layers can be identified based on the similarity of their mineral assemblage, morphology of glass shards, major and trace element contents, and isotopic ratios.

The group of tephra with high  $\text{K}_2\text{O}$  contents and high  $\text{Al}_2\text{O}_3/\text{Na}_2\text{O}$  ratios (pink symbols in Figures 3–7) are present in the northern half of our study area, and are distinguished by high LREE contents, low Zr/Nb ratios, as well as

high  $^{207}\text{Pb}/^{204}\text{Pb}$ ,  $^{206}\text{Pb}/^{204}\text{Pb}$ , and  $^{87}\text{Sr}/^{86}\text{Sr}$  ratios. Tephra layers mainly consist of pumiceous and blocky-shaped glass shards with a mineral assemblage of plg + amph  $\pm$  biot  $\pm$  qz. They mainly belong to the lithofacies 2 and 3 (Figure 2).

The group of tephra with low  $\text{K}_2\text{O}$  contents and low  $\text{Al}_2\text{O}_3/\text{Na}_2\text{O}$  ratios (blue symbols in Figures 3–7) are present in the southern half of our study area, and have low Nb and LREE contents, low La/Zr ratios, as well as high Zr/Yb and Rb/Th ratios. Tephra layers consist of glass shards of heterogeneous morphology with a mineral assemblage of plg + amph  $\pm$  qz, and they mainly belong to the lithofacies 4. The morphology of glass shards, the mineral composition and the spectrum of incompatible element of sample ATAC-47 (light blue symbol), are close to those of this group (Figures 3 and 6). However, ATAC-47 sample presents lower La/Yb, Zr/Yb, Rb/Th, Zr/Nb,  $^{207}\text{Pb}/^{204}\text{Pb}$ ,  $^{206}\text{Pb}/^{204}\text{Pb}$ , and  $^{87}\text{Sr}/^{86}\text{Sr}$  ratios (Figures 5 and 7). We therefore infer that this tephra layer belongs to another eruption.

The group of tephra with low  $\text{SiO}_2$  contents and low MgO/FeO ratios (orange symbols) are also present in the southern half of our study area, and present low Nb contents, and low Ba/Nb ratios. Glass shards are mainly bubble-wall-shaped with elongated vesicles. Tephra layers also contain plg + biot  $\pm$  qz and they mainly belong to the lithofacies 4. Tephra with medium  $\text{K}_2\text{O}$  contents and  $\text{Al}_2\text{O}_3/\text{Na}_2\text{O}$  ratios (yellow symbols) have a very similar signature than the previous group (Figures 2, 6 and 7) but they have been separated because they are more enriched in  $\text{SiO}_2$  (Figure 4), and present lower MgO/FeO and Zr/Nb ratios (Figures 4 and 5) and higher La/Zr ratios (Figure 5).

The two tephra with the low  $\text{SiO}_2$  contents and low MgO/FeO ratios (brown symbols) are present in the central part of our study area, and are distinguished by a large amount of lithics, a mixture between andesite and rhyolite blocky-shaped glass shards, low LREE contents and low Ba/Nb and  $^{206}\text{Pb}/^{204}\text{Pb}$ . Both tephra layers belong to the lithofacies 4.

Two samples have morphological and geochemical characteristics that do not allow us to correlate them with other tephra layers in the studied cores. Sample AMAD-41 (turquoise symbol), with high  $\text{K}_2\text{O}$  contents and high  $\text{Al}_2\text{O}_3/\text{Na}_2\text{O}$  ratios, is present at the northern limit of our study area. It has a significantly higher  $^{87}\text{Sr}/^{86}\text{Sr}$  ratio than other tephra layers (Figure 7b), and it is also distinguished from other samples in the Ba/La versus Zr/Nb diagram (Figure 5d). Sample AMAD-40 (green symbol) occurs in the north of our study area. It has the highest Ba/Nb, Ba/La, and Zr/Nb ratios, and the lowest  $^{207}\text{Pb}/^{204}\text{Pb}$  and  $^{87}\text{Sr}/^{86}\text{Sr}$  ratios.

### 5.3. Identification of the Source of Marine Tephra Layers Based on Their Major and Trace Element Contents and Sr-Pb Isotope Ratios

Measurements of major and trace element contents of marine tephra have been performed in this study on single glass shards. Very few measurements on single glass shards of Holocene tephra deposited onland in Ecuador and Colombia have been published. We have thus mainly compared our results with bulk tephra or whole-rock data obtained on pumices, blocks from pyroclastic flows, lava flows or scoria clasts (GEOROC database; <http://georoc.mpch-mainz.gwdg.de/>). Comparison of these two data sets should therefore be considered with caution, as the element contents of pristine glass and whole rock material can significantly differ depending on the mineral contents of the latter.

#### 5.3.1. High $\text{K}_2\text{O}$ —High $\text{Al}_2\text{O}_3/\text{Na}_2\text{O}$ Rhyolites

The volcanic source of tephra layers with the highest  $\text{K}_2\text{O}$  contents (>3 wt.%; Figure 4a) and high  $\text{Al}_2\text{O}_3/\text{Na}_2\text{O}$  ratios (>3.4; Figure 4b) may originate from volcanoes located in the Interandean Valley or the Eastern Cordillera of Ecuador, or in the Cordillera Central of Colombia (green, orange, and turquoise fields, respectively; Figures 1 and 4a). Considering volcanoes that experienced major eruptions during the Holocene, their source can therefore be Cotopaxi, Tungurahua and Soche volcanoes in Ecuador, and Azufral, Galeras, Cerro Machín and Nevado del Ruiz volcanoes in Colombia (Table 1).

The group of tephra belonging to the high-K series (pink circles; Figure 4a) presents the strongest enrichment in LILE and depletion in HREE (pink spectra; Figure 6) than other samples, typical of the Eastern Cordillera trend (e.g., Barragán et al., 1998; Hidalgo et al., 2012; Schiano et al., 2010). In addition, their Rb/Th ratios and Nb contents agree with a source located in the Eastern Cordillera (orange field; Figure 5e).  $^{206}\text{Pb}/^{204}\text{Pb}$ ,  $^{207}\text{Pb}/^{204}\text{Pb}$ , and  $^{87}\text{Sr}/^{86}\text{Sr}$  ratios obtained for AMAD-21, -34, -42 and ATAC-57 samples (pink points in Figure 7a) are significantly higher than those obtained on terrestrial volcanic products from Soche volcano (Figure 7a, red field in Figure 7c; Hidalgo et al., 2012;



Ancellin et al., 2017). This source is therefore discarded. Similarly, their  $^{87}\text{Sr}/^{86}\text{Sr}$  ratios are higher than those obtained for Tungurahua volcano (yellow field, Figure 7c; Nauret et al., 2018). On the contrary, their incompatible element spectra (pink field, Figure 6), as well as both  $^{207}\text{Pb}/^{204}\text{Pb}$  and  $^{87}\text{Sr}/^{86}\text{Sr}$  ratios, are close to the composition field obtained for products from the Chalupas caldera (pink field, Figure 7c; Ancellin et al., 2017; Bryant et al., 2006; Garrison et al., 2011). This caldera was not active during the Holocene, and therefore cannot be the source of marine tephra. However, the geochemical signature of products from the Colorado Canyon, located southeast of Cotopaxi volcano and dated at 4410–5320 cal BP (Table 1, Hall & Mothes, 2008b), is close to that of Chalupas caldera products (measured on single glass shards of the major ignimbrite deposit; Garrison et al., 2011). The mineralogy of onland deposits also agrees with the mineral assemblage identified in marine tephra layers (Table 1, Figure 3), and therefore confirms that these tephra layers may be associated with the *Colorado Canyon event*.

AMAD-41 sample, located in the northernmost core (KAMAF07; Figure 2a), is enriched in most of incompatible elements (turquoise spectra; Figure 6). As suggested by major element contents, this signature may correspond either to the Western Cordillera of Ecuador or to Colombian volcanism (Figure 4a). As it clearly plots in the Colombian volcanism composition field in the Ba/La versus Zr/Nb diagram, and it is close to it in the La/Yb versus Ba/Nb diagram (turquoise field; Figures 5a and 5d), AMAD-41 tephra should more likely originate from Colombia. In addition, AMAD-41 differs from other samples by a significantly higher  $^{87}\text{Sr}/^{86}\text{Sr}$  ratio (Figure 7b). Only Reventador volcano display such high value in Ecuador (Ancellin et al., 2017), but it presents significantly lower Pb isotope ratios than AMAD-41 (beige and green fields, respectively, Figure 7a), and no highly explosive eruptions of Reventador have been identified. Although few data are published for Colombian volcanoes (Chiaradia et al., 2020; Errázuriz-Henao et al., 2019; James & Murcia, 1984; Jaramillo et al., 2019; Laeger et al., 2013; Melson et al., 1990), both Pb and Sr isotope ratios obtained for AMAD-41 are consistent with those obtained for Cerro Machín volcano (Figure 7c). In addition, lava flows from the central dome of Cerro Machín volcano contain plagioclase, amphibole, quartz, and biotite phenocrysts with accessory Fe-Ti oxides, olivine and apatite (Laeger et al., 2013), consistent with the mineral assemblage observed for the AMAD-41 tephra layer (Figure 3a). The *Cerro Machín* volcano is thus thought to be the most likely source of this tephra, based on available data.

### 5.3.2. Low $\text{SiO}_2$ —High MgO/FeO Rhyolites

This group includes tephra samples with the lowest  $\text{SiO}_2$  content (<77 wt.%; Figure 4a).

Major element contents of tephra ATAC-45, -49, and -53 (i.e., orange symbols in Figures 4–6) suggest that they may originate from the Interandean Valley or the Eastern Cordillera of Ecuador (green and orange fields; Figures 1 and 4a). This is supported by their Nb contents and Rb/Th ratios typical of the Eastern Cordillera volcanoes (orange field, Figure 5e). Volcanoes from the Interandean Valley and the Eastern Cordillera that experienced at least one major Holocene eruption are Cotopaxi, Tungurahua and Soche volcanoes (Table 1). The trace element contents of products coming from these volcanoes are quite similar, and their compositional fields overlap (orange, yellow, and red fields, Figures 5a–5d), making marine tephra source identification uncertain. However,  $^{206}\text{Pb}/^{204}\text{Pb}$ ,  $^{207}\text{Pb}/^{204}\text{Pb}$ , and  $^{87}\text{Sr}/^{86}\text{Sr}$  ratios obtained for ATAC-45 and ATAC-59 samples (orange points in Figure 7) are significantly higher than those of onland volcanic products from Soche volcano (Figure 7a, red field in Figure 7c). Similarly, their  $^{207}\text{Pb}/^{204}\text{Pb}$  ratios are lower than those obtained for Tungurahua volcano (yellow field, Figure 7c). We can therefore discard both sources. ATAC-45, -49, and -53 marine tephra present a composition close to that of onland deposits of the “F rhyolite series” from Cotopaxi volcano (orange diamonds, which correspond to whole rock measurements performed on lava flows and pyroclastic fall deposits; Figure 4a) and a trace element signature also similar to the latter (orange field; Figure 6). Their Pb and Sr isotopic ratios are also consistent with values obtained at *Cotopaxi volcano* (Figures 7a and 7b, and orange field in Figure 7c), which is thus the most likely source.

Although ATAC-55 and ATAC-56 samples can be correlated based on their stratigraphic position, mineral assemblage, morphology of glass shards and bimodal composition (Figures 3 and 4a), their chemical composition is not homogeneous. Rhyolitic glass shards of ATAC-56 sample have a  $\text{K}_2\text{O}$  content of 3.0 wt.% suggesting a source in the Interandean Valley or the Eastern Cordillera of Ecuador (green and orange fields; Figures 1 and 4a), whereas those of ATAC-55 have a  $\text{K}_2\text{O}$  content of 2.1 wt.%, which is rather typical of the Western Cordillera of Ecuador (blue field; Figures 1 and 4a). However, their low incompatible element contents (brown samples, Figures 5e and 6) is characteristic of products from the Western Cordillera volcanoes. Their volcanic sources may therefore be Quilotoa, Atacazo-Ninahuilca, Pichincha, Pululahua, or Cuicocha volcanoes (Table 1). Quilotoa volcano cannot be the source of ATAC-55 and ATAC-56 due to the lack of biotite crystals in marine tephra (Figure 3a). In addition, our tephra presents  $^{87}\text{Sr}/^{86}\text{Sr}$  ratios higher than those obtained for Quilotoa and Pichincha products (Figures 7b and 7c).

Their  $^{207}\text{Pb}/^{204}\text{Pb}$  ratios are slightly higher than those obtained for Pululahua and Cuicocha volcanoes (brown and dark purple fields, Figure 7c). Pb and Sr ratios are in the range of values obtained for Atacazo-Ninahuilca volcano (blue fields, Figure 7c) and the mineral assemblage of both tephra layers is compatible with products of the latter (Table 1, Figure 3), but andesite glass shards are significantly more enriched in  $\text{K}_2\text{O}$  than Holocene pumices and blocks from pyroclastic flow deposits of Atacazo-Ninahuilca (blue squares, Figure 4a). Onland tephra layers identified along the coast in front of KAT20 coring site have been correlated to the  $\sim 710$  cal BP eruption of Quilotoa, the 2330–2600 cal BP activity of Pululahua, the 2320 cal BP eruption of Atacazo-Ninahuilca (N6 event) and the 4410–5320 or 6550–6800 cal BP Cotopaxi event (Vallejo Vargas, 2011). As explained above, Quilotoa and Cotopaxi volcanoes are not the source of ATAC-55 and ATAC-56 (Figure 2a). The 2330–2600 cal BP Pululahua and 2320 cal BP Atacazo-Ninahuilca events are therefore the most probable source of ATAC-55 and ATAC-56 tephra layers. However, both ages are inconsistent with the stratigraphic position of tephra, deposited only 4 cm above a foraminifera-rich layer dated at 4057–4237 cal BP (Figure 2a; Data Set S1). We therefore propose that ATAC-55 and ATAC-56 tephra layers have been reworked by turbidity currents shortly after 4057 cal BP. These currents appear to have remobilized older products from Atacazo-Ninahuilca (N5 or N4 event), and from at least one another unknown source whose products may belong to the medium-K calc-alkaline series (Figure 4a).

### 5.3.3. Medium $\text{K}_2\text{O}$ —Medium $\text{Al}_2\text{O}_3/\text{Na}_2\text{O}$ Rhyolites

This group includes tephra samples characterized by medium  $\text{K}_2\text{O}$  contents (2.5–3.5 wt.%; Figure 4a), medium  $\text{Al}_2\text{O}_3/\text{Na}_2\text{O}$  ratios (3.2–3.4; Figure 4b), and low  $\text{MgO}/\text{FeO}$  ratios ( $<0.25$ ; Figure 4b).

Although they bear higher  $\text{SiO}_2$  contents and lower  $\text{MgO}/\text{FeO}$  ratios, samples ATAC-46 and ATAC-50 (represented in yellow in Figures 4–6) have a geochemical signature close to that of samples ATAC-45, -46, and -53, correlated to the Cotopaxi volcano (orange spectra and orange field, Figure 6). Their trace element contents are consistent with a source located in the Eastern Cordillera (Figure 5e). In addition, the  $^{207}\text{Pb}/^{204}\text{Pb}$  and  $^{87}\text{Sr}/^{86}\text{Sr}$  ratio of sample ATAC-46 is close to the composition field obtained at Cotopaxi volcano (orange field, Figure 7c), and are different from the ranges of values obtained at Tungurahua and Soche volcanoes (yellow and red fields, Figure 7c). These data therefore suggest that ATAC-46 and ATAC-50 tephra layers are related to the *Cotopaxi volcano*.

The  $\text{K}_2\text{O}$  content of sample AMAD-40 suggests a source located in the Interandean Valley or in the Eastern Cordillera (green and orange fields, Figures 1a and 4a). However, its incompatible element contents (green spectra, Figure 6), as well as its Rb/Th ratio, are typical of volcanoes of the Western Cordillera of Ecuador (blue field; Figure 5e). Sample ATAC-40 clearly plots in the compositional field of Guagua Pichincha in the La/Yb versus Ba/Nb diagram (Figure 5a). Moreover, it presents the lowest  $^{207}\text{Pb}/^{204}\text{Pb}$  and  $^{87}\text{Sr}/^{86}\text{Sr}$  ratios (15.604 and 0.70404, respectively, Figure 7). Such values are only observed for products of *Pichincha volcano*, which is therefore the most likely source of this tephra layer.

### 5.3.4. Low $\text{K}_2\text{O}$ —Low $\text{Al}_2\text{O}_3/\text{Na}_2\text{O}$ Rhyolites

The volcanic source of tephra layers with the lowest  $\text{K}_2\text{O}$  content ( $<2.5$  wt.%; Figure 4a) and lowest  $\text{Al}_2\text{O}_3/\text{Na}_2\text{O}$  ratios ( $<3.3$ ; Figure 4b) may originate from the Western Cordillera of Ecuador (blue field; Figures 1 and 4a), and thus from Quilotoa, Atacazo-Ninahuilca, Pichincha, Pululahua or Cuicocha volcanoes (Table 1). As suggested by major elements, this group of tephra (i.e., blue symbols in Figures 4–6) exhibits Rb/Th ratios and Nb contents typical of the Western Cordillera (blue field, Figure 5e), and their Ba/La, Zr/Nb, La/Zr, and Rb/Th ratios are close to compositional fields of Atacazo-Ninahuilca, Cuicocha, Pichincha and Pululahua volcanoes (blue, dark purple, green, and brown fields, Figures 5b–5d). Samples ATAC-43, -51, -52, -58 and AMAD-37 have higher  $^{87}\text{Sr}/^{86}\text{Sr}$  and  $^{207}\text{Pb}/^{204}\text{Pb}$  ratios than volcanic products from Pichincha, Pululahua, and Cuicocha volcanoes (green, brown, and dark purple fields, respectively, Figure 7c). Their  $^{87}\text{Sr}/^{86}\text{Sr}$ ,  $^{207}\text{Pb}/^{204}\text{Pb}$ , and  $^{206}\text{Pb}/^{204}\text{Pb}$  ratios are in the range obtained onland for whole rock on pumices and blocks from pyroclastic flow deposits of *Atacazo-Ninahuilca volcano* (Barragán et al., 1998; Bourdon et al., 2003; Bryant et al., 2006; Hidalgo et al., 2012), which is therefore the most likely source for these samples. Sample ATAC-47 has a geochemical signature close to the latter, with slightly higher HREE contents (Figures 5 and 6). However, it presents lower  $^{207}\text{Pb}/^{204}\text{Pb}$ ,  $^{206}\text{Pb}/^{204}\text{Pb}$ , and  $^{87}\text{Sr}/^{86}\text{Sr}$  ratios (Figures 7a–7c), which indicate that its source may be Pululahua or Atacazo-Ninahuilca volcanoes (i.e., brown and blue fields in Figure 7c). The age of major eruptions of both volcanoes is inconsistent with the stratigraphic position of the tephra layer (i.e., slightly older than 4 ka; Figure 2a). Consequently, although ATAC-47 layer appears as primary deposit (Figure 2a), it may correspond to remobilized products from Atacazo-Ninahuilca (N5 or N4 event), and might include some ash from Pululahua volcano.

**Table 3**

*Comparison of Radiometric Ages Obtained on Onland Deposits (Given With 1- $\sigma$  Uncertainty, Calibration Details and Sources Given in Data Set S1) With Age Ranges Obtained on Foraminifera of Marine Deposits Below and Above Geochemically Correlated Marine Tephra Layers (i.e., the Most Restricted Time Period Considering All Age Constraints of Correlated Tephra Layers From a Same Event)*

Source	Eruption	<sup>14</sup> C age (cal BP, on onland deposits)	Correlated marine tephra layers	<sup>14</sup> C age constraint (cal BP, on marine deposits)
Atacazo-Ninahuilca	N5	4,880–4,940	ATAC-43, -44, -47*, -48, -51	Between 3,680–4,150 and 5,050–5,460
	N4	6,140–6,310	ATAC-52, -58 AMAD-37	Between 5,730–6,110 and 6,590–6,990
Guagua Pichincha	10th century	960–1,000	AMAD-40	<2,040–2,480
Cerro Machín	Espartillal-P0 eruptive events	4,840–5,730	AMAD-41	>3,880–4,330
Cotopaxi	Colorado canyon	4,410–5,320	ATAC-57, -59 AMAD-21, -22, -24, -29, -34, -35, -36, -39	Between 4,530–4,970 and 5,304–5,680
			AMAD-42	<5,890–6,250
	F4	6,550–6,800	ATAC-45, -49, -53	Between 6,590–6,990 and 7,140–7,480
	F2	7,160–8,600	ATAC-46, -50	Between 7,140–7,480 and 8,780–92,40
Unknown			ATAC-55, -56	<3,970–4,420

*Note.* Sample AMAD-47 marked with an asterisk (\*) maybe a mixture between tephra from Atacazo-Ninahuilca N5 event and another volcano.

#### 5.4. Age of Marine Tephra Layers

Based on both stratigraphic position of tephra layers in the cores and available <sup>14</sup>C age data, we can infer a time window for the deposition of the tephra layers, and thus an age estimate of each eruption. As it is difficult to establish a precise age model for tephra layers due to variable sedimentation rate and the presence of erosive and rapidly emplaced deposits from gravity flows, we constrain the minimum and maximum age of each tephra (Table 3).

Tephra layers belonging to Atacazo-Ninahuilca eruptions occur in cores from the southern half of the study area (light blue and blue layers, Figure 8a). In KAT18 core, ATAC-51 tephra is located between foraminifera-rich layers dated at 3217–3516 (0.60 mbsf) and 5725–6110 (1.69 mbsf) cal BP. Similarly, ATAC-52 tephra is located between foraminifera-rich layers dated at 5725–6110 (1.69 mbsf) and 6588–6986 (1.38 mbsf) cal BP, suggesting that tephra layers result from two different eruptions. The location and stratigraphic position of ATAC-48 (located above a layer dated at 5049–5462 cal BP in core KAT17), ATAC-44 (located above a layer dated at 5148–5553 cal BP in core KAT16) and ATAC-43 (located between layers dated at 4238–4689 and 6024–6403 cal BP in core KAT15) tephra layers suggest a single eruption, and correlate to that recorded by ATAC-51. Similarly, ATAC-58 tephra layer (core KAT21) and AMAD-37 pod (core KAMA02), located below a foraminifera-rich layer dated at 5403–5788 cal BP (8.20 mbsf), and above a layer dated at 14507–15083 cal BP (2.15 mbsf), respectively, is older and rather correlates to the eruption recorded by ATAC-52 layer. The age of ATAC-47 tephra (core KAT17) is constrained by two layers dated at 3676–4146 (3.14 mbsf) and 5049–5462 cal BP (5.73 mbsf).

The tephra layer associated with Guagua Pichincha activity, AMAD-40 pod (0.48–0.49 mbsf in core KAMA19), is stratigraphically above a layer dated at 2042–2483 cal BP (3.68 mbsf), and thus corresponds to the youngest volcanic deposit. We consider that the stratigraphic position of tephra pods may slightly differ from that of the original tephra layer, as pods are evidence of burrows formed below the primary deposit (e.g., Hopkins et al., 2020; Kutterolf, Freundt, Hansteen, et al., 2021).

The northernmost tephra layer (AMAD-41, core KAMAf07), whose geochemical signature is close to that of the Colombian Cerro Machín volcano, is located 60 cm below a layer dated at 3880–4329 cal BP. The age of the eruption is therefore poorly constrained, and occurred at least 4.3 ka ago.

The five tephra layers with a geochemical composition similar to that of Cotopaxi products can be separated into two groups (orange and yellow samples, Figures 4–8). ATAC-45 and ATAC-49 samples (orange layers, Figure 8a) are stratigraphically above ATAC-46 and ATAC-50 samples (yellow layers, Figure 8a) in cores KAT16 and KAT17, respectively (Table 1), and therefore represent a younger eruptive event. Foraminifera-rich layers

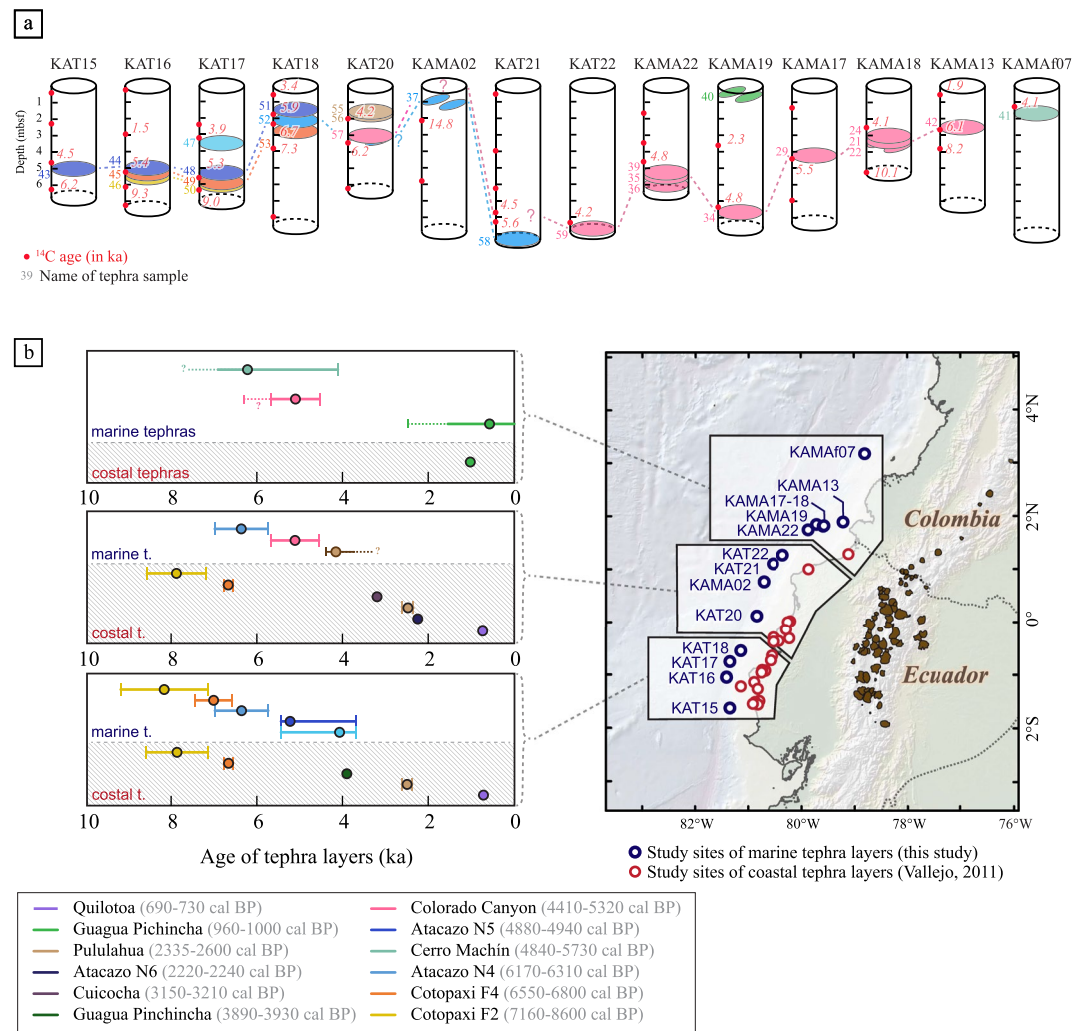


**Figure 8.** (a) Tephrostratigraphy of the studied Holocene tephra layers recorded in *Amadeus* and *Atacames* marine cores. Radiometric ages are detailed in Figure 2a and Data Set S1. Coring sites are shown with blue circles in Figure 7b. Colors of tephra layers correspond to symbols of Figure 7b. Brown (55–56) and light blue (47) tephra layers correspond to a secondary deposit that has reworked Atacazo N4 and/or N5 tephra layers and tephra from another source. (b) Synthesis of the radiometric age of tephra identified in marine (blue circles; this study) and coastal (red circles; Vallejo Vargas, 2011) sediments. The error bar corresponds to the 1- $\sigma$  uncertainty of <sup>14</sup>C age for coastal tephra and to the minimal and maximal age constraints for marine tephra, summarized in Table 3.

dated at 6588–6986 (2.38 mbsf) and 7138–7477 cal BP (3.88 mbsf) in core KAT18 constrain the deposition age of ATAC-45, -49, and -53 tephra layers. ATAC-46 and ATAC-50 have therefore been emitted between 7138 and 7477 cal BP and 8775–9238 cal BP (core KAT17, 6.21 mbsf).

In KAT20 core, ATAC-55 (1.83 mbsf) and ATAC-56 (1.89 mbsf) tephra layers, whose geochemistry suggests a mixture of remobilized products from Atacazo-Ninahuilca and from at least one unknown source, have been emplaced after a foraminifera-rich layer dated at 3973–4422 cal BP (1.93 mbsf).

Finally, the 11 tephra layers with a homogeneous geochemical composition (Figures 4–8) and associated with the Colorado Canyon event are present in the northern part of the study area (pink layers, Figure 8a). AMAD-34 tephra lies below a layer dated at 4525–4970 cal BP in KAMA19 core, and AMAD-29 tephra lies above a layer dated at 5304–5681 cal BP in KAMA 17 core. The stratigraphic position of ATAC-57 (core KAT20), ATAC-59 (core KAT22), AMAD-35-36-39 (core KAMA22), and AMAD-21, -22, -24 (core KAMA18) tephra layers strongly agrees with this age range (Figure 8a). AMAD-42 (core KAMA13, 2.54–2.57 mbsf) tephra layer appears slightly older, lying above a layer dated at 5888–6252 cal BP (2.66 mbsf) within hemipelagic marine sediments.

### 5.5. Land-Sea Correlations of Distal Tephra Fallout Deposits Based on Comparison of Their Age and Geochemical Signature With Proximal Volcanic Products

In this section, we use volcanic sources determined using mineralogy, geochemical and isotopic signatures together with the age range of marine tephra horizons off Ecuador to propose a first land-sea correlation of marine tephra with major Holocene eruptions in the Northern Andes.

The geochemical signature of the northernmost tephra is typical of Colombian volcanism (AMAD-41 sample from core KAMAf07, represented in turquoise in Figures 4–8), and has been associated with the activity of *Cerro Machín*. It lies 60 cm below a layer dated at 3880–4329 cal BP (Figure 8) and may therefore correspond to the Espartillal or P0 eruptive events that occurred between 4840 and 5730 cal BP (Rueda, 2005; Thouret et al., 1995). Unfortunately, the age of deposition of this tephra is poorly constrained, and no chemical data of products of Espartillal or P0 eruptive events have been published. Consequently, correlating the AMAD-41 tephra to one of these eruptions remains unresolved.

The age, mineral assemblage and geochemistry of the group of tephra layers with the highest incompatible element contents and Pb-Sr isotopes (i.e., AMAD-21, -22, -24, -29, -34, -35, -36, -39, -42 and ATAC-57 samples from cores KAMA13, 17, 18, 19, 22 and KAT20, pink symbols in Figures 2a, 6, 7 and 8a), suggest that they correspond to the 4410–5320 cal BP event of *Colorado Canyon*, from Cotopaxi volcano. AMAD-42 sample probably emplaced slightly earlier, and may be associated with an early eruptive stage, with a limited dispersion of deposits. No deposits associated with the Colorado Canyon event are present in KAMA02 and KAT21 cores (Figure 7a). Primary layers may have remobilized and dispersed by bioturbation or gravity flows, but magnetic susceptibility data do not suggest the presence of cryptotephra in these cores (Gonzalez, 2018; Ratzov, 2009). We identified three tephra layers from this eruption in both KAMA18 and KAMA22 cores (Figure 2a). As these cores are free of any turbidite layers interbedded with tephra layers, we propose that AMAD-24 and AMAD-39 tephra layers represent a diffused upper boundary tail caused by bioturbation or remobilization of thin particles by a debris flow, respectively (Ratzov, 2009), whereas AMAD-36 tephra layer may represent a diffused lower boundary tail induced by bioturbation (e.g., Abbott et al., 2018; Gudmundsdóttir et al., 2011).

The mineral assemblage and geochemistry of AMAD-40 sample (core KAMA19) are similar to Holocene proximal products of Pichincha volcano (green symbols, Figures 6, 7 and 8a). The stratigraphic position of the marine tephra layer suggest that it was emplaced during the *tenth century eruption of Guagua Pichincha* (Robin et al., 2008). This correlation concurs with the dispersion of products of this eruption toward the NNW, and distal tephra layers identified on onshore marine terraces (Vallejo Vargas, 2011), and in a drill core collected on the southeast flank of the Cerro Negro volcano (Santamaría et al., 2017), near the Colombia border (Figure 2a).

Characterized by a mineral assemblage and geochemical signature typical of magmas from *Cotopaxi volcano*, ATAC-45, -49, -53 and ATAC-46, -50 samples (orange and yellow symbols in Figures 4–8a), retrieved in cores KAT16, 17 and 18, have been correlated to this latter. Their stratigraphic position and  $^{14}\text{C}$  age of pelagic foraminifers (Figure 2a) suggest that they have been emitted during the 6550–6800 cal BP F4 and 7160–8600 cal BP F2 events, which are associated with the largest volumes of emitted products by Cotopaxi volcano (Hall & Mothes, 2008b). In addition, this correlation is in agreement with that of Vallejo Vargas (2011), who associated 14 10–100 cm-thick and six 5–100 cm-thick tephra layers located between the Esmeraldas province and the south of the Manta Peninsula (Figure 1b), with Cotopaxi's F4 and F2 rhyolitic episodes, respectively. However, the age assigned to these coastal tephra layers should be considered with caution, as studied sections lack absolute dating, and the compositions of the “F rhyolitic episodes” products are similar (Vallejo Vargas, 2011). Lonsdale (1978) described an ash-rich turbidite sequence between 4.4 and 4.1 mbsf covered by 4 m of hemipelagic mud in a core collected in the trench, 35 km N and 25 km NW of KAT17 and KAT18 coring sites, respectively (Figure 2a). Despite the lack of geochemical data, this sequence may be correlated to ATAC-47, -48, -49, and -50 tephra from KAT17 core.

ATAC-43, -44, -48, -51, -52, -58 and AMAD-37 samples, retrieved in cores KAT15, 16, 17, 18, and 21, and KAMA02, ranging from latitudes  $\sim 1.5^\circ\text{S}$  to  $1.2^\circ\text{N}$ , present both mineral assemblage and geochemical signature typical of *Atacazo-Ninahuilca volcano* (Figures 4–7), and their stratigraphic position together with  $^{14}\text{C}$  age determinations suggest that they have been emplaced during the  $\sim 4.9$  and  $\sim 6.2$  ka N4 events (Hidalgo et al., 2008; dark and light blue symbols, respectively, Figure 8a). No deposits from the latter were sampled in the KAT20 core, but Gonzalez (2018) observed a tephra pod between the ATAC-57 tephra layer (associated with the 4410–5320 cal BP Colorado Canyon event) and the 3.47 mbsf hemipelagic layer dated at  $6240 \pm 190$  cal BP (Data Set S1), that

may be associated with the N4 eruption. Sample AMAD-47 is located above AMAD-48 layer (Figure 8a). Consequently, either it corresponds to a younger eruption than that of AMAD-48, or it corresponds to an older eruption whose deposits were reworked and deposited shortly before 3.9 ka. The stratigraphic position of ATAC-47 sample is inconsistent with Atacazo-Ninahuilca N6 (2220–2240 cal BP) eruption. We therefore suggest that AMAD-47 layer may correspond to remobilized products from Atacazo-Ninahuilca N5 (4880–4940 cal BP) event, and might include some ash from another source as Pululahua volcano.

Although sedimentary deposits interbedded with tephra layers of ATAC-55 and ATAC-56 samples (core KAT20; Figure 2a) are hemipelagic, the morphology of glass shards, as well as the heterogeneous nature and composition of grains, suggest some reworking (e.g., Abbott et al., 2018; Gudmundsdóttir et al., 2011) shortly after ~4 ka (Figure 2a). They contain plagioclase and amphibole crystals, and their geochemical signature is close to that of Atacazo products (Figures 4–7). However, abundant lithics, andesite glass shards, as well as Sr and Pb isotope ratios (Figure 7), suggest a mixing with distal tephra fallouts from one or more other unknown sources, whose products may belong to the medium-K calc-alkaline series.

Figure 8b compares the age of tephra layers identified in marine cores (this study) with those identified along the coast (Vallejo Vargas, 2011). It shows evidences that some volcanic events have been recorded in the coastal sediments but not in marine sediments analyzed in this work, such as the eruptions of Quilotoa, N6 Atacazo-Ninahuilca, Pululahua, and Cuicocha (~710, ~2230, 2335–2600, and ~3180 cal BP, respectively). The estimated sedimentation rates to the south of our study area, where deposits from Quilotoa are expected to be present, are particularly low. Consequently, tephra deposits associated with the 710 cal BP Quilotoa event and located at very low depths within the cores might have been disturbed or even eliminated during the coring, or the distal fallout may not have been recorded in sediments of the continental slope. Lonsdale (1977) also documented strong bottom currents that may have transported and/or dispersed tephra northward. Vallejo Vargas (2011) correlated only one 8 cm-thick tephra layer to the Cuicocha eruption. This VEI-4 event had a minor impact on the coastal zone (Vallejo Vargas, 2011), and distal deposits may not have been recorded due to floating pumices. Lack of tephra from the ~2230 cal BP N6 event of Atacazo-Ninahuilca and ~3910 cal BP Guagua Pichincha eruptions in marine sediments may be explained by the restricted distribution of their respective products, deposited in the direction of the fairly isolated KAT15 core for the ~3910 cal BP Guagua Pichincha eruption, and between KAT20 and KAMA02 cores for the N6 event. Products from the 2335–2600 cal BP event of Pululahua volcano have been identified between 0.5°N and 1.5°S on onshore marine terraces (Vallejo Vargas, 2011). No tephra layers younger than 3.9 ka is present in KAT15, 16, 17, and 18 cores (Figure 8a). If products from this event reached the ocean, they may have been dispersed by deep ocean currents (e.g., Lonsdale, 1977). In the Jama Valley, in front of KAT20 coring site, Zeidler and Pearsall (1994) identified three tephra layers, which constitute chronological markers of human settlement for archeology studies. However, there are no geochemical analyses for source identification of these tephra emplaced at  $1890 \pm 110$ ,  $3610 \pm 40$ , and  $3930 \pm 60$  cal BP (Zeidler & Pearsall, 1994; Data Set S1).

In the archeological site of La Maná, 40 km ESE of Quilotoa volcano (Figures 2a), Guillaume-Gentil (2008) identified nine tephra layers, deposited during the last 15 kyr. Based on radiocarbon ages, they have been attributed to Quilotoa (1150–1300 and 16300–15100 cal BCE), Atacazo-Ninahuilca (110–410 and 1210–760 cal BCE), Cotopaxi (1130–830 cal BCE), Cuicocha (1450–1100 cal BCE), and Tungurahua (1130–830 cal BCE) volcanoes. Products from Tungurahua volcano bear scarce or no amphibole crystals (e.g., Hall et al., 1999). As marine tephra layers that do not contain any amphibole crystals have a geochemical signature close to that of Cotopaxi products, this source can be discarded for our tephra layers. No spectra of incompatible elements compare to the signature of Soche volcano, which was also active during the Holocene. As we found no evidence that any tephra layer in our core collection is sourced at Quilotoa, Cuicocha, Tungurahua, and Soche volcanoes, their products may not have reached the sea, left no tephra record in our study sites, or may have been transported outside our study area by winds and ocean currents (e.g., Lonsdale, 1977).

On the contrary, some volcanic events recorded in marine sediments have not been identified in coastal terraces, such as the tephra layer offshore Colombia correlated to products from Cerro Machín volcano (AMAD-41 sample), as well as N5 and N6 events of Atacazo-Ninahuilca (~4910 and ~6240 cal BP, respectively), and the Colorado Canyon event from Cotopaxi volcano. No continental cores or study sites are located in the area of core KAMAf07 (Figure 8b), which could explain why deposits associated with the AMAD-41 sample have not been identified onland. In coastal study sites where deposits of N5 and N6 events are supposed to be present, deposits located at depth equivalent to 5–6 ka are terrigenous with shells or bioturbation, clayed, arenitic, alluvial, or do

not crop out (Vallejo Vargas, 2011). As marine tephra layers are particularly thin, varying between <1 and 3 cm (Text S1 in Supporting Information S2), we assume that onland deposits have not been preserved because of the smaller eruption volumes. Furthermore, products from the F rhyolite series of Cotopaxi present similar composition and geochemical signatures, which prevents to accurately determine the eruption associated with distal deposits. Coastal tephra layers associated with Cotopaxi products are composed of glass shards with abundant plagioclase and biotite crystals, as well as some quartz and scarce amphibole crystals. Based on their stratigraphic position and geochemical signature they have been attributed to the strongest events of the F series, that is, the 7160–8600 cal BP F2 and 6550–6800 cal BP F4 events (Vallejo Vargas, 2011), but new geochemical analyses performed on coastal tephra layers indicate that some of them were emitted during the Colorado Canyon event (S. Vallejo, personal communication).

In addition, Figure 8b showed evidences that the oldest deposits are located in the southernmost study sites, while the youngest are mainly distributed in the central and northern region, which may show a slight change in wind direction from ESE to NE during the Holocene. Considering eruptive records evidenced in this study and distal tephra fallouts identified on onshore marine terraces (Vallejo Vargas, 2011), products of at least 12 VEI-4 to 6 eruptions reached the Ecuadorian and south Colombian margins for the past ~8 kyr (Figure 8b), which corresponds to a return rate of about 1.5 major explosive event per millennium.

Finally, we identified marine tephra layers deposited between turbidite beds emplaced during large past earthquakes (Figure 2a; Ratzov et al., 2010; Migeon et al., 2017). Although beyond the scope of this manuscript, these tephra layers can be used to constrain the timing of such events. The determination of the geochemical signature and Sr-Pb isotope data of tephra from major eruptions performed in this work also provide time constraints for human settlement in archeological sites presenting tephra deposits (e.g., Guillaume-Gentil, 2008; Zeidler & Pearsall, 1994). Such eruptions have buried many agricultural fields and triggered migration of pre-Columbian inhabitants (Hall & Mothes, 2008a; Le Pennec et al., 2013), and illustrate the high volcanic hazard associated with the explosive volcanism of Ecuador.

### 5.6. Tephra Dispersal and Size of Major Holocene Eruptions

Our correlation of distal tephra samples to dated Holocene eruptions in the Ecuadorian Cordilleras allows us to map the sites where each tephra isochron is recorded in distal sediments. The resulting maps reveal a NW distribution for the 980 cal BP Guagua Pichincha tephra deposit, consistent with the plume direction inferred from thickness data in proximal areas (Figure 9a). The tephra fall covers  $2.8 \times 10^4$  km<sup>2</sup> within the 1 cm isopach, and tephra have been transported until 250 km from their source. Distal deposits from other large Holocene eruptions (Ninahuilca 4910 cal BP and two events from Cotopaxi) display westerly dispersal patterns that are also supported by proximal thickness data at both volcanoes (Figures 9b–9d). This is a typical situation in the Ecuadorian region where prevailing winds of the Inter-Tropical Convergence Zone blow from the Amazonian lowlands toward the Pacific Ocean, that is, from East to West. We estimate the distribution area for the Ninahuilca 4910 cal BP event to be  $2.0 \times 10^4$  km<sup>2</sup>, and tephra have been spread out as far as 290 km from the eruptive center. The widespread dispersal patterns evidenced at Cotopaxi, when compared to the seemingly narrower dispersal of the Atacazo-Ninahuilca eruption, suggest tephra columns of higher energy and some possible wind-shift effects during eruptions of the former ice-clad Cotopaxi volcano. The area within the 1 cm isopach is  $6.3 \times 10^4$  and  $8.2 \times 10^4$  km<sup>3</sup> for the 6550–6800 and 7160–8600 cal BP event, respectively, and tephra have reached regions located more than 350 km away from the Cotopaxi volcano.

These distal inland-coastal and offshore tephra records yield constraints to appraise the size of the associated eruptions. Our tephra thickness data, however, must be considered with caution. Indeed, the inland volcanic tephra may have been partly eroded or accumulated by winds or running waters after eruption and before being overlain by younger deposits. Similarly, tephra emplaced in marine sediments may have undergone some tectonic disturbance and slumping on the Ecuadorian margin, while tephra in the trench area may have been partly or totally redistributed by ocean deep-sea currents (e.g., Freundt et al., 2021; Hopkins et al., 2020; Kutterolf, Freundt, Druitt, et al., 2021; Lowe, 2011; Wetzel, 2009). On the other hand, our data are all above 1 cm in thickness in the reconstructed depositional area of each eruption. We therefore delineated the sub-elliptical envelope of all sites where each tephra has been identified to trace a proxy of the 1 cm isopach (dashed lines in Figure 9). We determined the area of the latter using the ArcGIS software (Table S1) and used the single isopach approach of Legros (2000) to infer the minimal tephra volume of each layer, which ranges from 0.4 to 5.6 km<sup>3</sup> (Figure 10a, details in Table S1).

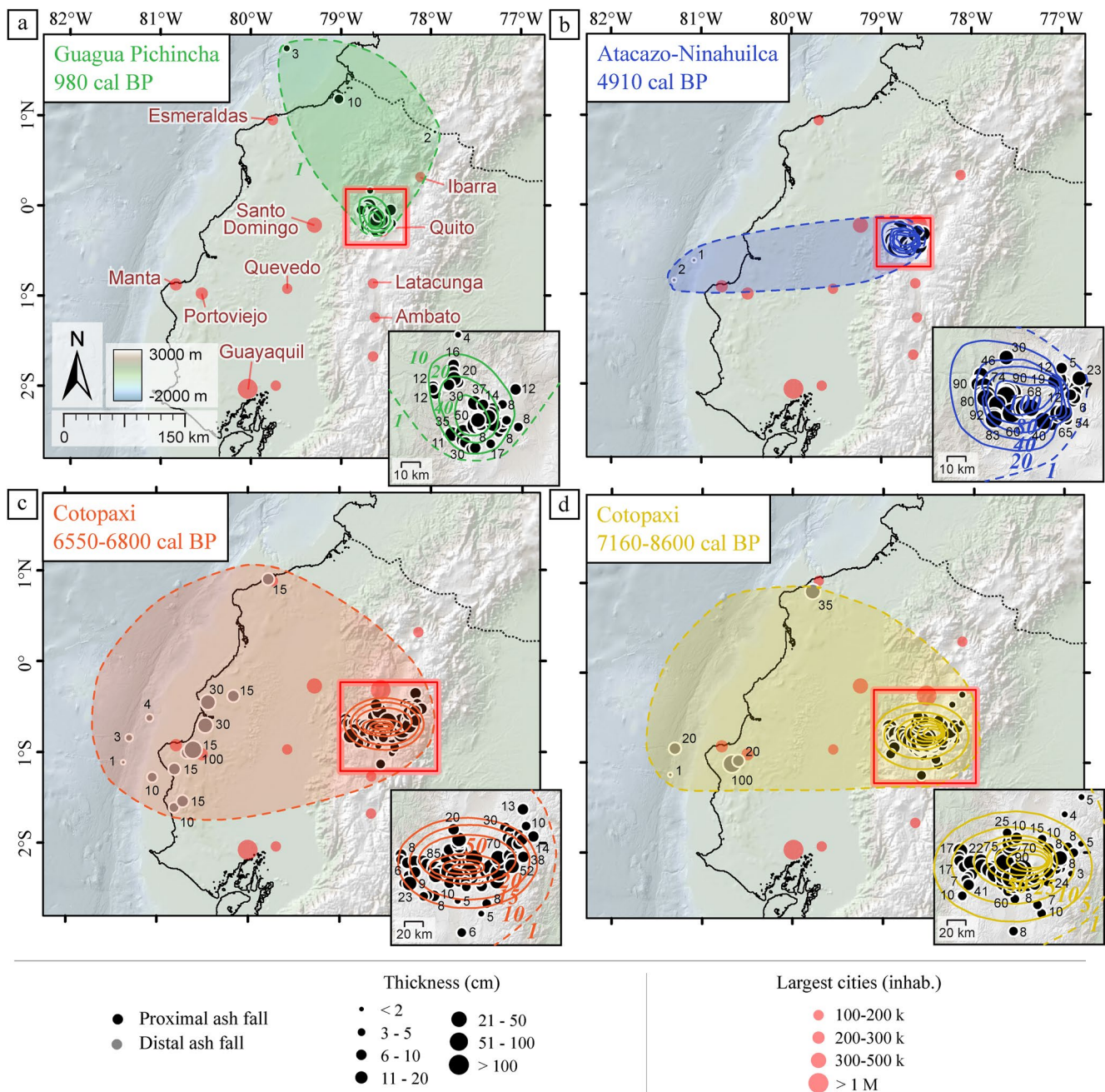


**Figure 9.** Isopach maps of large Holocene eruption from Ecuadorian volcanoes, whose products have been correlated in marine cores. Contour lines of isopach maps in the Cordillera are from Robin et al. (2008), Hidalgo et al. (2008), Hall and Mothes (2008b), and Santamaría et al. (2017), and in the coastal region from Vallejo Vargas (2011). Thickness of tephra are indicated by black and gray points for proximal and distal deposits, whose deposition mechanisms are different and can impact volume calculations. We do not consider ATAC-55 and ATAC-56 tephra layers, as they appear to be reworked and as their source is not well defined. The location of largest cities is indicated by red points.

To examine the general thickness decay rate of the tephra layers, we merged our data with those of the literature in a classical plot  $\text{Log}(\text{thickness})$  versus  $(\text{isopach area})^{1/2}$  (Figure 10b). We obtain a best fit for our data sets using an exponential thinning rate with two or three breaks-in-slope (Figure 10b; Bonadonna & Houghton, 2005). Results obtained for Guagua Pichincha and Atacazo-Ninahuilca deposits (1.3 and 2.1 km<sup>3</sup>, respectively) are slightly higher than previous estimates based on proximal deposits. In contrast, tephra volumes obtained for Cotopaxi tephra layers (5.0 km<sup>3</sup> for the 6550–6800 cal BP event, and 6.0 km<sup>3</sup> for the 7160–8600 cal BP event, Figure 10a) are lower than previous estimates but of the same order of magnitude. These new volume estimates are slightly



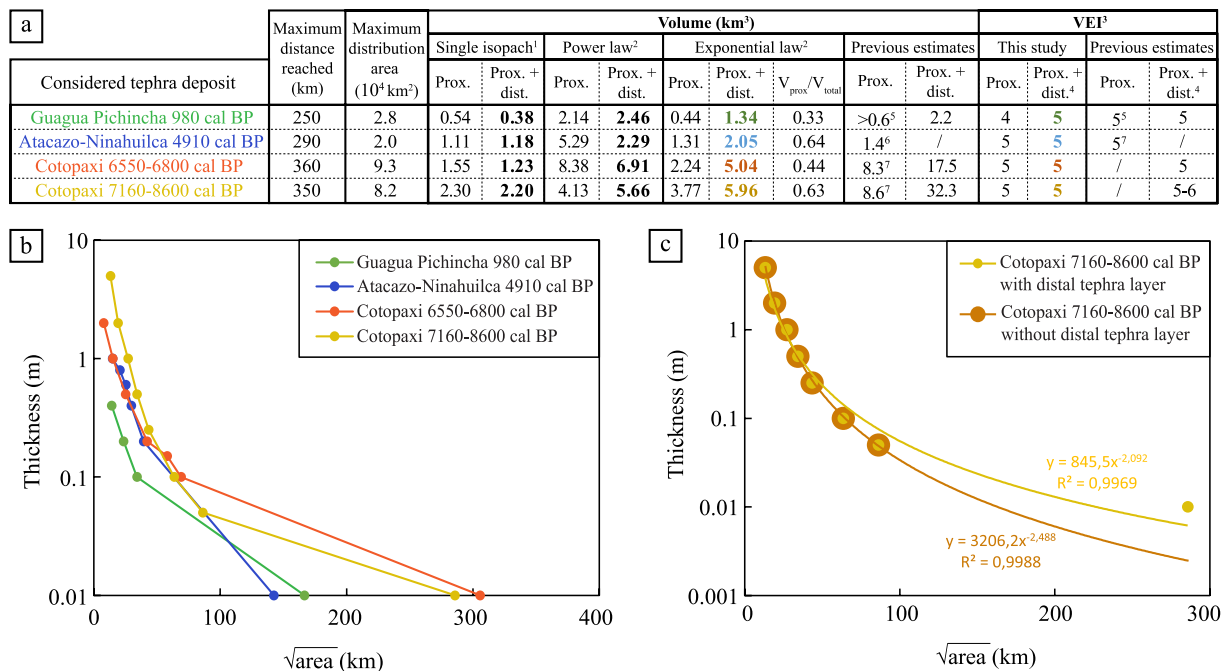


**Figure 10.** Estimated deposit volumes of volcanic events identified in marine cores and their associated Volcanic Explosivity Index (VEI). (a) Summary table of estimated deposit volumes and VEI calculated using different approaches (<sup>1</sup>Legros, 2000; <sup>2</sup>Bonadonna and Houghton, 2005; <sup>3</sup>Newhall and Self, 1982), and compared to previous estimates (<sup>4</sup>Vallejo Vargas, 2011; <sup>5</sup>Robin et al., 2008; <sup>6</sup>Hidalgo, 2006; <sup>7</sup>Hall and Mothes, 2008b). Prox.: proximal; dist.: distal. (b) Thickness of deposits versus square root of isopach area for selected eruptions. (c) Thickness of deposits versus square root of isopach area for Cotopaxi F2 event. Yellow and orange lines are power law trend curves that best fit the data that consider, or not, the most distal isopach (1 cm-thick; Figure 9), respectively. It highlights that the best approach in our cases is a multi-trend from exponential law equation for each of segment between two breaks-in-slope in a logarithm of tephra thickness versus square root of isopach area (Figure 9b; Bonadonna & Houghton, 2005).

lower than that obtained in Chile for the 1932 CE eruptions of Quizapu (9.5 and 4.1 km<sup>3</sup> for DRE volume, Hildreth & Drake, 1992) and similar to the ~11.7 ka eruption of Mentolat (~1.8 km<sup>3</sup>, Weller et al., 2019) volcanoes. However, they are significantly lower than the largest known Quaternary eruption of the Northern Volcanic Zone of the Andes, the 216 ± 5 ka eruption of the Chalupas caldera in Ecuador, whose total bulk deposit volume of both ignimbrite and co-ignimbrite amounts to ~230 km<sup>3</sup> (Bablon, Quidelleur, Siani et al., 2020). Accordingly, our revised estimates of the VEI for these events lend support to previous determinations (the ~980 cal BP Guagua Pichincha eruption is raised to VEI-5, Figure 10a). This in turn confirms that eruption size determined solely from distal tephra deposits can provide relevant proxies for tephra volume estimates, notably when data from proximal deposits are unavailable.

## 6. Conclusion

This work on marine tephra layers provides new insights into the source and spatial distribution of deposits from major Holocene volcanic events that reached the Ecuadorian and Southern Colombian margins. We identified 28 tephra layers in 14 marine cores collected between 3°N and 2°S during *Amadeus* and *Atacames* surveys. The morphology of glass shards, as well as the mineral assemblage, major and trace element content and Sr-Pb isotope ratios of each tephra, have been characterized in detail. Based on comparison with the geochemical signature of onland deposits together with the stratigraphic position of marine tephra layers and temporal constraints provided by <sup>14</sup>C age determinations, we performed the first land-sea correlation of volcanic products in Ecuador. Such correlation of tephra layers allows us to improve the catalog of eruptions that affected the coastal zone during the Holocene, and thus to specify the frequency of major eruptions whose products are stratigraphically recorded beyond 200 km away from their sources. We highlight that products emitted during at least seven eruptions from four Ecuadorian and Colombian volcanoes (Guagua Pichincha, Atacazo-Ninahuilca, Cotopaxi, and Cerro Machín) reached the offshore during the Holocene. With both eruptive records evidenced in this study and distal tephra fallouts identified on onshore marine terraces (Vallejo Vargas, 2011), we obtain for eruption size in the

range of VEI-4 to 6 a return rate of about 1.5 event per millennium for the past 8 kyr. We propose new eruptive tephra volumes of 1.3–6.0 km<sup>3</sup> for the four largest eruptions at the Columbian-Ecuadorian volcanic arc taking into account distal tephra distribution. The mineral assemblage and the geochemical composition of tephra layers, together with their age deduced from onshore deposits, accurately described in this study, constitute robust chronostratigraphic markers that can be used to identify the age of tephra or sedimentary sequences present in future coring, and for which <sup>14</sup>C age determination are not possible. This study of the Plio-Quaternary tephrochronology in Ecuador is a first step to better document the recurrence rate of major eruptions and the long-term evolution of magma geochemistry.

## Data Availability Statement

The location of coring sites, depth of tephra layers, results of radiocarbon ages, as well as raw electron microprobe, LA-ICP-MS and ICP-AES results are archived and available at Zenodo data repository (<https://doi.org/10.5281/zenodo.7016623>).

## References

- Abbott, P. M., Griggs, A. J., Bourne, A. J., & Davies, S. M. (2018). Tracing marine cryptotephra in the North Atlantic during the last glacial period: Protocols for identification, characterisation and evaluating depositional controls. *Marine Geology*, *401*, 81–97. <https://doi.org/10.1016/j.margeo.2018.04.008>
- Almeida, M. (2016). *Estudio petrográfico y geoquímico del volcán Cotacachi – provincia de Imbabura, Ecuador* (PhD thesis). Escuela Politécnica Nacional.
- Ancellin, M.-A., Samaniego, P., Vlastélic, I., Nauret, F., Gannoun, A., & Hidalgo, S. (2017). Across-arc versus along-arc Sr-Nd-Pb isotope variations in the Ecuadorian volcanic arc. *Geochemistry, Geophysics, Geosystems*, *18*(3), 1163–1188. <https://doi.org/10.1002/2016GC006679>
- Andrade, S. D., Müller, A. V., Vasconez, F. J., Beate, B., Aguilar, J., & Santamaría, S. (2021). Pululahu dome complex, Ecuador: Eruptive history, total magma output and potential hazards. *Journal of South American Earth Sciences*, *106*, 103046. <https://doi.org/10.1016/j.jsames.2020.103046>
- Bablon, M., Quidelleur, X., Samaniego, P., Le Pennec, J.-L., Audin, L., Jomard, H., et al. (2019). Interactions between volcanism and geodynamics in the southern termination of the Ecuadorian arc. *Tectonophysics*, *751*, 54–72. <https://doi.org/10.1016/j.tecto.2018.12.010>
- Bablon, M., Quidelleur, X., Samaniego, P., Le Pennec, J.-L., Lahitte, P., Liorzou, C., et al. (2018). Eruptive chronology of Tungurahua volcano (Ecuador) revisited based on new K-Ar ages and geomorphological reconstructions. *Journal of Volcanology and Geothermal Research*, *357*, 378–398. <https://doi.org/10.1016/j.jvolgeores.2018.05.007>
- Bablon, M., Quidelleur, X., Samaniego, P., Le Pennec, J.-L., Santamaría, S., Liorzou, C., et al. (2020). Volcanic history reconstruction in northern Ecuador: Insights for eruptive and erosion rates on the whole Ecuadorian arc. *Bulletin of Volcanology*, *82*(1), 11. <https://doi.org/10.1007/s00445-019-1346-1>
- Bablon, M., Quidelleur, X., Siani, G., Samaniego, P., Le Pennec, J.-L., Nouet, J., et al. (2020). Glass shard K-Ar dating of the Chalupas caldera major eruption: Main Pleistocene stratigraphic marker of the Ecuadorian volcanic arc. *Quaternary Geochronology*, *57*, 101053. <https://doi.org/10.1016/j.quageo.2020.101053>
- Barbante, C., Kehrwald, N. M., Marianelli, P., Vinther, B. M., Steffensen, J. P., Cozzi, G., et al. (2013). Greenland ice core evidence of the 79 AD Vesuvius eruption. *Climate of the Past*, *9*(3), 1221–1232. <https://doi.org/10.5194/cp-9-1221-2013>
- Barberi, F., Coltelli, M., Ferrara, G., Innocenti, F., Navarro, J. M., & Santacroce, R. (1988). Plio-Quaternary volcanism in Ecuador. *Geochemical Magazine*, *125*, 1–14. <https://doi.org/10.1017/s001675680009328>
- Barberi, F., Coltelli, M., Frullani, A., Rosi, M., & Almeida, E. (1995). Chronology and dispersal characteristics of recently (last 5000 years) erupted tephra of Cotopaxi (Ecuador): Implications for long-term eruptive forecasting. *Journal of Volcanology and Geothermal Research*, *69*(3–4), 217–239. [https://doi.org/10.1016/0377-0273\(95\)00017-8](https://doi.org/10.1016/0377-0273(95)00017-8)
- Barragán, R., Geist, D., Hall, M., Larson, P., & Kurz, M. (1998). Subduction controls on the compositions of lavas from the Ecuadorian Andes. *Earth and Planetary Science Letters*, *154*(1–4), 153–166. [https://doi.org/10.1016/S0012-821X\(97\)00141-6](https://doi.org/10.1016/S0012-821X(97)00141-6)
- Beate, B. (1994). *El Soche: Un volcán activo en la Provincia de Sucumbios, Ecuador – Primeros datos descriptivos* (Abstracts. Terceras Jornadas en Ciencias de la Tierra, pp. 9–10). Facultad de Geología, La Escuela Politécnica Nacional.
- Bernard, B., & Andrade, D. (2011). Volcanes Cuaternarios del Ecuador Continental. Map 1:500000.
- Bluth, G. J. S., Doiron, S. D., Schnetzler, C. C., Krueger, A. J., & Walter, L. S. (1992). Global tracking of the SO<sub>2</sub> clouds from the June, 1991 Mount Pinatubo eruptions. *Geophysical Research Letters*, *19*(2), 151–154. <https://doi.org/10.1029/91GL02792>
- Bonadonna, C., & Houghton, B. F. (2005). Total grain-size distribution and volume of tephra-fall deposits. *Bulletin of Volcanology*, *67*(5), 441–456. <https://doi.org/10.1007/s00445-004-0386-2>
- Bouma, A. H. (1962). *Sedimentology of some flysch deposits: A graphic approach to facies interpretation* (pp. 168). Elsevier.
- Bourdon, E., Eissen, J. P., Gutscher, M. A., Monzier, M., Hall, M. L., & Cotten, J. (2003). Magmatic response to early aseismic ridge subduction: The Ecuadorian margin case (South America). *Earth and Planetary Science Letters*, *205*(3–4), 123–128. [https://doi.org/10.1016/s0012-821x\(02\)01024-5](https://doi.org/10.1016/s0012-821x(02)01024-5)
- Brichau, S., Reyes, P., Gautheron, C., Hernández, M. J., Michaud, F., Leisen, M., et al. (2021). First timing constraints on the Ecuadorian Coastal Cordillera exhumation: Geodynamic implications. *Journal of South American Earth Sciences*, *105*, 103007. <https://doi.org/10.1016/j.jsames.2020.103007>
- Bryant, J. A., Yogodzinski, G. M., Hall, M. L., Lewicki, J. L., & Bailey, D. G. (2006). Geochemical constraints on the origin of volcanic rocks from the Andean Northern Volcanic Zone, Ecuador. *Journal of Petrology*, *47*(6), 1147–1175. <https://doi.org/10.1093/petrology/egl006>
- Calvache, M. L., Cortés, J. G. P., & Williams, S. N. (1997). Stratigraphy and chronology of the Galeras volcanic complex, Colombia. *Journal of Volcanology and Geothermal Research*, *77*(1–4), 5–19. [https://doi.org/10.1016/S0377-0273\(96\)00083-2](https://doi.org/10.1016/S0377-0273(96)00083-2)
- Calvache, M. L. V. (1990). Pyroclastic deposits of the November 13, 1985 eruption of Nevado del Ruiz volcano, Colombia. *Journal of Volcanology and Geothermal Research*, *41*(1–4), 67–78. [https://doi.org/10.1016/0377-0273\(90\)90083-R](https://doi.org/10.1016/0377-0273(90)90083-R)

- Calvache, M. L. V., & Williams, S. N. (1997). Geochemistry and petrology of the Galeras Volcanic Complex, Colombia. *Journal of Volcanology and Geothermal Research*, 77(1–4), 21–38. [https://doi.org/10.1016/S0377-0273\(96\)00084-4](https://doi.org/10.1016/S0377-0273(96)00084-4)
- Carey, S. (1997). Influence of convective sedimentation on the formation of widespread tephra fall layers in the deep sea. *Geology*, 9, 839–842. [https://doi.org/10.1130/0091-7613\(1997\)025<0839:iocot>2.3.co;2](https://doi.org/10.1130/0091-7613(1997)025<0839:iocot>2.3.co;2)
- Castilla, S. C., Pardo, N., Larrea, P., Zuluaga, C. A., Sarmiento, S., Noguera, D., & Sarmiento, G. A. (2019). Pre-eruptive conditions and pyroclastic emplacement of the last known vulcanian eruption of Azufral Volcano, SW Colombia. *Journal of South American Earth Sciences*, 91, 372–386. <https://doi.org/10.1016/j.jsames.2018.08.007>
- Chiaradia, M., Barnes, J. D., & Cadet-Voisin, S. (2014). Chlorine stable isotope variations across the Quaternary volcanic arc of Ecuador. *Earth and Planetary Science Letters*, 396, 22–33. <https://doi.org/10.1016/j.epsl.2014.03.062>
- Chiaradia, M., Müntener, O., & Beate, B. (2020). Effects of aseismic ridge subduction on the geochemistry of frontal arc magmas. *Earth and Planetary Science Letters*, 531, 115984. <https://doi.org/10.1016/j.epsl.2019.115984>
- Chiaradia, M., Müntener, O., Beate, B., & Fontignie, D. (2009). Adakite-like volcanism of Ecuador: Lower crust magmatic evolution and recycling. *Contributions to Mineralogy and Petrology*, 158(5), 563–588. <https://doi.org/10.1007/s00410-009-0397-2>
- Collot, J.-Y., Agudelo, W., Ribodetti, A., & Marcaillou, B. (2008). Origin of a crustal splay fault and its relation to the seismogenic zone and underplating at the erosional north Ecuador–south Colombia oceanic margin. *Journal of Geophysical Research: Solid Earth*, 113(B12), B12102. <https://doi.org/10.1029/2008jb005691>
- Collot, J.-Y., Marcaillou, B., Sage, F., Michaud, F., Agudelo, W., Charvis, P., et al. (2004). Are rupture zone limits of great subduction earthquakes controlled by upper plate structures? Evidence from multichannel seismic reflection data acquired across the northern Ecuador–southwest Colombia margin. *Journal of Geophysical Research*, 109(B11), B11103. <https://doi.org/10.1029/2004JB003060>
- Collot, J.-Y., Michaud, F., Alvarado, A., Marcaillou, B., Sosson, M., Ratzov, G., et al. (2009). Vision general de la morfología submarina del margen convergente de Ecuador-Sur de Colombia: Implicaciones sobre la transferencia de masa y la edad de la subducción de la Cordillera de Carnegie. In J.-Y. Collot, V. Sallares, & N. Pazmino (Eds.), *Geología y geofísica marina y terrestre del Ecuador: desde la costa continental hasta las Islas Galápagos* (pp. 47–74). CNDM, IRD, INOCAR.
- Collot, J.-Y., Migeon, S., Spence, G., Legonidec, Y., Marcaillou, B., Schneider, J.-L., et al. (2005). Seafloor margin map helps in understanding subduction earthquakes. *Eos, Transactions American Geophysical Union*, 86(46), 463–465. <https://doi.org/10.1029/2005eo460003>
- Collot, J.-Y., Ratzov, G., Silva, P., Proust, J.-N., Migeon, S., Hernandez, M.-J., et al. (2019). The Esmeraldas Canyon: A helpful marker of the Pliocene–Pleistocene tectonic deformation of the North Ecuador – Southwest Colombia convergent margin. *Tectonics*, 38(8), 3140–3166. <https://doi.org/10.1029/2019TC005501>
- Collot, J.-Y., Sanclemente, E., Nocquet, J.-M., Leprêtre, A., Ribodetti, A., Jarrin, P., et al. (2017). Subducted oceanic relief locks the shallow megathrust in central Ecuador. *Journal of Geophysical Research: Solid Earth*, 122(5), 3286–3305. <https://doi.org/10.1002/2016JB013849>
- Coronel, J. (2002). *Les canyons de la marge équatorienne : approche morphostructurale et évolution* (MSc thesis). Université de Nice Sophia Antipolis.
- Cotten, J., Le Dez, A., Bau, M., Caroff, M., Maury, R. C., Dulski, P., et al. (1995). Origin of anomalous rare-earth element and yttrium enrichments in subaerially exposed basalts: Evidence from French Polynesia. *Chemical Geology*, 119(1–4), 115–138. [https://doi.org/10.1016/0009-2541\(94\)00102-e](https://doi.org/10.1016/0009-2541(94)00102-e)
- Derkachev, A. N., Gorbarenko, S. A., Ponomareva, V. V., Portnyagin, M. V., Malakhova, G. I., & Liu, Y. (2020). Middle to late Pleistocene record of explosive volcanic eruptions in marine sediments offshore Kamchatka (Meiji Rise, NW Pacific). *Journal of Quaternary Science*, 35(1–2), 362–379. <https://doi.org/10.1002/jqs.3175>
- Droux, A., & Delaloye, M. (1996). Petrography and geochemistry of Plio-Quaternary calc-alkaline volcanoes of Southwestern Colombia. *Journal of South American Earth Sciences*, 9(1–2), 27–41. [https://doi.org/10.1016/0895-9811\(96\)00025-9](https://doi.org/10.1016/0895-9811(96)00025-9)
- Errázuriz-Henao, C., Gómez-Tuena, A., Duque-Trujillo, J., & Weber, M. (2019). The role of subducted sediments in the formation of intermediate mantle-derived magmas from the Northern Colombian Andes. *Lithos*, 336–337, 151–168. <https://doi.org/10.1016/j.lithos.2019.04.007>
- Freundt, A., Schindlbeck-Belo, J. C., Kutterolf, S., & Hopkins, J. L. (2021). Tephra layers in the marine environment: A review of properties and emplacement processes. *Geological Society, London, Special Publications*, 520(1), SP520–2021–50. <https://doi.org/10.1144/SP520-2021-50>
- Galer, S. J. G., & Abouchami, W. (1998). Practical application of lead triple spiking for correction of instrumental mass discrimination. *Mineralogical Magazine*, 62A(1), 491–492. <https://doi.org/10.1180/minmag.1998.62a.1.260>
- Garrison, J., Davidson, J., Reid, M., & Turner, S. (2006). Source versus differentiation controls on U-series disequilibria: Insights from Cotopaxi Volcano, Ecuador. *Earth and Planetary Science Letters*, 244(3–4), 548–565. <https://doi.org/10.1016/j.epsl.2006.02.013>
- Garrison, J. M., Davidson, J. P., Hall, M., & Mothes, P. (2011). Geochemistry and petrology of the Most recent deposits from Cotopaxi Volcano, Northern Volcanic Zone, Ecuador. *Journal of Petrology*, 52(9), 1641–1678. <https://doi.org/10.1093/petrology/egr023>
- Goldfinger, C., Morey, A. E., Nelson, C. H., Gutiérrez-Pastor, J., Johnson, J. E., Karabanov, E., et al. (2007). Rupture lengths and temporal history of significant earthquakes on the offshore and north coast segments of the Northern San Andreas Fault based on turbidite stratigraphy. *Earth and Planetary Science Letters*, 254(1–2), 9–27. <https://doi.org/10.1016/j.epsl.2006.11.017>
- Gonzalez, M. (2018). *Nature and origin of sedimentary deposits in the Ecuador subduction trench: Paleoseismological implications* (PhD thesis). Université de Rennes 1.
- Gourgaud, A., & Thouret, J.-C. (1990). Magma mixing and petrogenesis of the 13 November 1985 eruptive products at Nevado del Ruiz (Colombia). *Journal of Volcanology and Geothermal Research*, 41(1–4), 79–96. [https://doi.org/10.1016/0377-0273\(90\)90084-S](https://doi.org/10.1016/0377-0273(90)90084-S)
- Graindorge, D., Calahorra, A., Charvis, P., Collot, J.-Y., & Bethoux, N. (2004). Deep structures of the Ecuador convergent margin and the Carnegie Ridge, possible consequence on great earthquakes recurrence interval. *Geophysical Research Letters*, 31(4), L04603. <https://doi.org/10.1029/2003GL018803>
- Gudmundsdóttir, E. R., Eiriksson, J., & Larsen, G. (2011). Identification and definition of primary and reworked tephra in Late Glacial and Holocene marine shelf sediments off North Iceland. *Journal of Quaternary Science*, 26(6), 589–602. <https://doi.org/10.1002/jqs.1474>
- Guillaume-Gentil, N. (2008). Cinq mille ans d'histoire au pied des volcans en Équateur. *Terra Archeologica* VI.
- Hall, M. L., & Mothes, P. A. (1994). Tefrostratigrafía holocénica de los volcanes principales del valle interandino, Ecuador. *Estudios de geografía*, 6, 47–67.
- Hall, M. L., & Mothes, P. A. (2008a). Quilotoa volcano – Ecuador: An overview of young dacitic volcanism in a lake-filled caldera. *Journal of Volcanology and Geothermal Research*, 176(1), 44–55. <https://doi.org/10.1016/j.jvolgeores.2008.01.025>
- Hall, M. L., & Mothes, P. A. (2008b). The rhyolitic–andesitic eruptive history of Cotopaxi volcano, Ecuador. *Bulletin of Volcanology*, 70(6), 675–702. <https://doi.org/10.1007/s00445-007-0161-2>
- Hall, M. L., & Mothes, P. A. (2008c). Volcanic impediments in the progressive development of pre-Columbian civilizations in the Ecuadorian Andes. *Journal of Volcanology and Geothermal Research*, 176(3), 344–355. <https://doi.org/10.1016/j.jvolgeores.2008.01.039>

- Hall, M. L., Robin, C., Beate, B., Mothes, P., & Monzier, M. (1999). Tungurahua Volcano, Ecuador: Structure, eruptive history and hazards. *Journal of Volcanology and Geothermal Research*, 91, 1–21. [https://doi.org/10.1016/s0377-0273\(99\)00047-5](https://doi.org/10.1016/s0377-0273(99)00047-5)
- Hall, M. L., Samaniego, P., Le Penneç, J. L., & Johnson, J. B. (2008). Ecuadorian Andes volcanism: A review of Late Pliocene to present activity. *Journal of Volcanology and Geothermal Research*, 176, 1–6. <https://doi.org/10.1016/j.jvolgeores.2008.06.012>
- Hall, M. L., & Wood, C. A. (1985). Volcano-tectonic segmentation of the northern Andes. *Geology*, 13(3), 203–207. [https://doi.org/10.1130/0091-7613\(1985\)13<203:vsotna>2.0.co;2](https://doi.org/10.1130/0091-7613(1985)13<203:vsotna>2.0.co;2)
- Hernández, M. J., Michaud, F., Collot, J. Y., Proust, J. N., & d'Acremont, E. (2020). Evolution of the Ecuador offshore nonaccretionary forearc basin and margin segmentation. *Tectonophysics*, 781, 228374. <https://doi.org/10.1016/j.tecto.2020.228374>
- Hidalgo, S. (2006). *Les interactions entre magmas calco-alcalins "classiques" et adakitiques : Exemple du complexe volcanique Atacazo-Ninahuilca (Equateur)* (PhD thesis). Université Blaise Pascal-Clermont-Ferrand II.
- Hidalgo, S., Battaglia, J., Arellano, S., Sierra, D., Bernard, B., Parra, R., et al. (2018). Evolution of the 2015 Cotopaxi eruption revealed by combined geochemical and seismic observations. *Geochemistry, Geophysics, Geosystems*, 19(7), 2087–2108. <https://doi.org/10.1029/2018GC007514>
- Hidalgo, S., Gerbe, M. C., Martin, H., Samaniego, P., & Bourdon, E. (2012). Role of crustal and slab components in the Northern Volcanic Zone of the Andes (Ecuador) constrained by Sr–Nd–O isotopes. *Lithos*, 132(133), 180–192. <https://doi.org/10.1016/j.lithos.2011.11.019>
- Hidalgo, S., Monzier, M., Almeida, E., Chazot, G., Eissen, J.-P., van der Plicht, J., & Hall, M. L. (2008). Late Pleistocene and Holocene activity of the Atacazo–Ninahuilca Volcanic Complex (Ecuador). *Journal of Volcanology and Geothermal Research*, 176(1), 16–26. <https://doi.org/10.1016/j.jvolgeores.2008.05.017>
- Hildreth, W., & Drake, R. E. (1992). Volcan Quizápu, Chilean Andes. *Bulletin of Volcanology*, 54(2), 93–125. <https://doi.org/10.1007/bf00278002>
- Hopkins, J. L., Wysoczanski, R. J., Orpin, A. R., Howarth, J. D., Strachan, L. J., Lunenburg, R., et al. (2020). Deposition and preservation of tephra in marine sediments at the active Hikurangi subduction margin. *Quaternary Science Reviews*, 247, 106500. <https://doi.org/10.1016/j.quascirev.2020.106500>
- Jacobs, C. T., Goldin, T. J., Collins, G. S., Piggott, M. D., Kramer, S. C., Melosh, H. J., et al. (2015). An improved quantitative measure of the tendency for volcanic ash plumes to form in water: Implications for the deposition of marine ash beds. *Journal of Volcanology and Geothermal Research*, 290, 114–124. <https://doi.org/10.1016/j.jvolgeores.2014.10.015>
- James, D. E., & Murcia, L. A. (1984). Crustal contamination in northern Andean volcanics. *Journal of the Geological Society*, 141(5), 823–830. <https://doi.org/10.1144/gsjgs.141.5.0823>
- Jaramillo, J. S., Cardona, A., Monsalve, G., Valencia, V., & León, S. (2019). Petrogenesis of the late Miocene Combia volcanic complex, north-western Colombian Andes: Tectonic implication of short term and compositionally heterogeneous arc magmatism. *Lithos*, 330(331), 194–210. <https://doi.org/10.1016/j.lithos.2019.02.017>
- Jochum, K. P., Nohl, U., Herwig, K., Lammel, E., Stolland, B., & Hofmann, A. W. (2005). GeoReM: A new geochemical database for reference materials and isotopic standards. *Geostandards and Geoanalytical Research*, 29(3), 333–338. <https://doi.org/10.1111/j.1751-908x.2005.tb00904.x>
- Kutterolf, S., Freundt, A., Druitt, T. H., McPhie, J., Nomikou, P., Pank, K., et al. (2021). The medial offshore record of explosive volcanism along the Central to Eastern Aegean volcanic arc: 2. Tephra ages and volumes, eruption magnitudes and marine sedimentation rate variations. *Geochemistry, Geophysics, Geosystems*, 22(12), e2021GC010011. <https://doi.org/10.1029/2021GC010011>
- Kutterolf, S., Freundt, A., Hansteen, T. H., Dettbarn, R., Hampel, F., Sievers, C., et al. (2021). The medial offshore record of explosive volcanism along the Central to Eastern Aegean volcanic arc: 1. Tephrostratigraphic correlations. *Geochemistry, Geophysics, Geosystems*, 22(12), e2021GC010010. <https://doi.org/10.1029/2021GC010010>
- Kutterolf, S., Schindlbeck, J. C., Anselmetti, F. S., Ariztegui, D., Brenner, M., Curtis, J., et al. (2016). A 400-ka tephrochronological framework for Central America from Lake Petén Itzá (Guatemala) sediments. *Quaternary Science Reviews*, 21, 200–220. <https://doi.org/10.1016/j.quascirev.2016.08.023>
- Lacasse, C., & van den Bogaard, P. (2002). Enhanced airborne dispersal of silicic tephra during the onset of Northern Hemisphere glaciations, from 6 to 0 Ma records of explosive volcanism and climate change in the subpolar North Atlantic. *Geology*, 30(7), 623–626. [https://doi.org/10.1130/0091-7613\(2002\)030<0623:eado>2.0.co;2](https://doi.org/10.1130/0091-7613(2002)030<0623:eado>2.0.co;2)
- Laeger, K., Halama, R., Hansteen, T., Savov, I. P., Murcia, H. F., Cortés, G. P., & Garbe-Schönberg, D. (2013). Crystallization conditions and petrogenesis of the lava dome from the ~900 years BP eruption of Cerro Machín Volcano, Colombia. *Journal of South American Earth Sciences*, 48, 193–208. <https://doi.org/10.1016/j.jsames.2013.09.009>
- Legros, F. (2000). Minimum volume of tephra fallout deposit estimated from a single isopach. *Journal of Volcanology and Geothermal Research*, 96(1–2), 25–32. [https://doi.org/10.1016/s0377-0273\(99\)00135-3](https://doi.org/10.1016/s0377-0273(99)00135-3)
- Le Penneç, J.-L., De Saulieu, G., Samaniego, P., Jaya, D., & Gailler, L. (2013). A devastating Plinian eruption at Tungurahua volcano reveals Formative occupation at ~1100 cal BC in Central Ecuador. *Radiocarbon*, 55(3–4), 1199–1214. [https://doi.org/10.2458/azu\\_js\\_rc.55.16225](https://doi.org/10.2458/azu_js_rc.55.16225)
- Le Penneç, J.-L., Jaya, D., Samaniego, P., Ramón, P., Moreno Yáñez, S., Egred, J., & van der Plicht, J. (2008). The AD 1300–1700 eruptive periods at Tungurahua volcano, Ecuador, revealed by historical narratives, stratigraphy and radiocarbon dating. *Journal of Volcanology and Geothermal Research*, 176(1), 70–81. <https://doi.org/10.1016/j.jvolgeores.2008.05.019>
- Loayza, G., Proust, J.-N., Michaud, F., & Collot, J.-Y. (2013). Évolution pléistocène du système de canyons du Golfe de Guayaquil (Équateur). Contrôles paléo-climatique et tectonique [Abstract]. *14e congrès français de sédimentologie*, Paris, France.
- Lonsdale, P. (1977). Inflow of bottom water to the Panama Basin. *Deep-Sea Research*, 24(12), 1065–1101. [https://doi.org/10.1016/0146-6291\(77\)90514-8](https://doi.org/10.1016/0146-6291(77)90514-8)
- Lonsdale, P. (1978). Ecuadorian Subduction System. *AAPG Bulletin*, 62, 2454–2477. <https://doi.org/10.1306/C1EA5526-16C9-11D7-8645000102C1865D>
- Lowe, D. J. (2011). Tephrochronology and its application: A review. *Quaternary Geochronology*, 6(2), 107–153. <https://doi.org/10.1016/j.quageo.2010.08.003>
- Manville, V., & Wilson, C. J. N. (2004). Vertical density currents: A review of their potential role in the deposition and interpretation of deep-sea ash layers. *Journal of the Geological Society*, 161(6), 947–958. <https://doi.org/10.1144/0016-764903-067>
- Marcaillou, B., & Collot, J.-Y. (2008). Chronostratigraphy and tectonic deformation of the North Ecuadorian–South Colombian offshore Manglares forearc basin. *Marine Geology*, 255(1–2), 30–44. <https://doi.org/10.1016/j.margeo.2008.07.003>
- Marcaillou, B., Collot, J.-Y., Ribodetti, A., d'Acremont, E., Mahamat, A.-A., & Alvarado, A. (2016). Seamount subduction at the North-Ecuadorian convergent margin: Effects on structures, inter-seismic coupling and seismogenesis. *Earth and Planetary Science Letters*, 433, 146–158. <https://doi.org/10.1016/j.epsl.2015.10.043>
- Marcaillou, B., Spence, G., Wang, K., Collot, J.-Y., & Ribodetti, A. (2008). Thermal segmentation along the N. Ecuador–S. Colombia margin (1–4°N): Prominent influence of sedimentation rate in the trench. *Earth and Planetary Science Letters*, 272(1–2), 296–308. <https://doi.org/10.1016/j.epsl.2008.04.049>

- Marriner, G. F., & Millward, D. (1984). The petrology and geochemistry of Cretaceous to recent volcanism in Colombia: The magmatic history of an accretionary plate margin. *Journal of the Geological Society*, 141(3), 473–486. <https://doi.org/10.1144/gsjgs.141.3.0473>
- Martin, H., Moya, J.-F., Guitreau, M., Blichert-Toft, J., & Le Pennec, J.-L. (2014). Why Archaean TTG cannot be generated by MORB melting in subduction zones. *Lithos* 198–199, 1–13. <https://doi.org/10.1016/j.lithos.2014.02.017>
- Melson, W. G., Allan, J. F., Jerez, D. R., Nelen, J., Calvache, M. L., Williams, S. N., et al. (1990). Water contents, temperatures and diversity of the magmas of the catastrophic eruption of Nevado del Ruiz, Colombia, November 13, 1985. *Journal of Volcanology and Geothermal Research*, 41(1–4), 97–126. [https://doi.org/10.1016/0377-0273\(90\)90085-T](https://doi.org/10.1016/0377-0273(90)90085-T)
- Michaud, F., Collot, J.-Y., Alvarado, A., López, E., & el personal científico y técnico del INOCAR. (2006). *República del Ecuador, Batimetría y Relieve Continental*. Publicación IOA-CVM-02-Post, INOCAR.
- Michaud, F., Proust, J. N., Collot, J. Y., Lebrun, J. F., Witt, C., Ratzov, G., et al. (2015). Quaternary sedimentation and active faulting along the Ecuadorian shelf: Preliminary results of the ATACAMES Cruise (2012). *Marine Geophysical Researches*, 36(1), 81–98. <https://doi.org/10.1007/s11001-014-9231-y>
- Migeon, S., Garibaldi, C., Ratzov, G., Schmidt, S., Collot, J.-Y., Zaragosi, S., & Texier, L. (2017). Earthquake-triggered deposits in the subduction trench of the north Ecuador/south Colombia margin and their implication for paleoseismology. *Marine Geology*, 384, 47–62. <https://doi.org/10.1016/j.margeo.2016.09.008>
- Mothes, P. A., & Hall, M. L. (2008). The plinian fallout associated with Quilotoa's 800 yr BP eruption, Ecuadorian Andes. *Journal of Volcanology and Geothermal Research*, 176(1), 56–69. <https://doi.org/10.1016/j.jvolgeores.2008.05.018>
- Mountney, N. P., & Westbrook, G. K. (1997). Quantitative analysis of Miocene to recent forearc basin evolution along the Colombian margin. *Basin Research*, 9(3), 177–196. <https://doi.org/10.1046/j.1365-2117.1997.00040.x>
- Murcia, H. F., Hurtado, B. O., Cortés, G. P., Macías, J. L., & Cepeda, H. (2008). The ~2500 yr B.P. Chicoral non-cohesive debris flow from Cerro Machín Volcano, Colombia. *Journal of Volcanology and Geothermal Research*, 171(3–4), 201–214. <https://doi.org/10.1016/j.jvolgeores.2007.11.016>
- Myers, M. L., Geist, D. J., Rowe, M. C., Harpp, K. S., Wallace, P. J., & Dufek, J. (2014). Replenishment of volatile-rich mafic magma into a degassed chamber drives mixing and eruption of Tungurahua volcano. *Bulletin of Volcanology*, 76(11), 872. <https://doi.org/10.1007/s00445-014-0872-0>
- Nakajima, T., & Kanai, Y. (2000). Sedimentary features of seismoturbidites triggered by the 1983 and older historical earthquakes in the eastern margin of the Japan Sea. *Sedimentary Geology*, 135(1–4), 1–19. [https://doi.org/10.1016/S0037-0738\(00\)00059-2](https://doi.org/10.1016/S0037-0738(00)00059-2)
- Nauret, F., Samaniego, P., Ancellin, M.-A., Tournigand, P.-Y., Le Pennec, J.-L., Vlastelic, I., et al. (2018). The genetic relationship between andesites and dacites at Tungurahua volcano, Ecuador. *Journal of Volcanology and Geothermal Research*, 349, 283–297. <https://doi.org/10.1016/j.jvolgeores.2017.11.012>
- Nelson, C. S., Froggatt, P. C., & Gosson, G. J. (1985). Nature, chemistry, and origin of late Cenozoic megascopic tephra in Leg 90 cores from the southwest Pacific. In J. P. Kennett, & C. C. von der Borch, et al. (Eds.), *Initial Reports of the Deep Sea Drilling Project* (Vol. 90, pp. 1160–1173). U.S. Govt. Printing Office.
- Newhall, C. G., & Self, S. (1982). Volcanic Explosivity Index (VEI): An estimate of explosive magnitude for historical volcanism. *Journal of Geophysical Research*, 87(C2), 1231–1238. <https://doi.org/10.1029/jc087ic02p01231>
- Nocquet, J.-M., Villegas-Lanza, J. C., Chlieh, M., Mothes, P. A., Rolandone, F., Jarrin, P., et al. (2014). Motion of continental slivers and creeping subduction in the northern Andes. *Nature Geoscience*, 7(4), 287–291. <https://doi.org/10.1038/ngeo2099>
- Opdyke, N. D., Hall, M., Mejia, V., Huang, K., & Foster, D. A. (2006). Time-averaged field at the equator: Results from Ecuador. *Geochemistry, Geophysics, Geosystems*, 7(11), Q11005. <https://doi.org/10.1029/2005GC001221>
- Papale, P., & Rosi, M. (1993). A case of no-wind plinian fallout at Pululagua caldera (Ecuador): Implications for models of clast dispersal. *Bulletin of Volcanology*, 55(7), 523–535. <https://doi.org/10.1007/BF00304594>
- Pedoja, K., Dumont, J. F., Lamothe, M., Ortlieb, L., Collot, J.-Y., Ghaleb, B., et al. (2006). Plio-Quaternary uplift of the Manta peninsula and La Plata Island and the subduction of the Carnegie Ridge, central coast of Ecuador. *Journal of South American Earth Sciences*, 22(1–2), 1–21. <https://doi.org/10.1016/j.jsames.2006.08.003>
- Pin, C., & Gannoun, A. (2017). Integrated extraction chromatographic separation of the lithophile elements involved in long-lived radiogenic isotope systems (Rb-Sr, U-Th-Pb, Sm-Nd, La-Ce, and Lu-Hf) useful in geochemical and environmental sciences. *Analytical Chemistry*, 89(4), 2411–2417. <https://doi.org/10.1021/acs.analchem.6b04289>
- Proust, J. N., Martillo, C., Michaud, F., Collot, J. Y., & Dauteuil, O. (2016). Subduction of seafloor asperities revealed by a detailed stratigraphic analysis of the active margin shelf sediments of Central Ecuador. *Marine Geology*, 380, 345–362. <https://doi.org/10.1016/j.margeo.2016.03.014>
- Ramón, P., Vallejo, S., Mothes, P., Andrade, D., Vásquez, F., Yepes, H., et al. (2021). Instituto Geofísico – Escuela Politécnica Nacional, the Ecuadorian Seismology and Volcanology Service. *Volcanica*, 4(S1), 93–112. <https://doi.org/10.30909/vol.04.S1.93112>
- Ratzov, G. (2009). *Processus gravitaires sous-marins le long de la zone de subduction Nord Equateur – Sud Colombie : Apports à la connaissance de l'érosion tectonique et de la déformation d'une marge active, et implications sur l'aléa tsunamis* (PhD thesis). Université de Nice-Sophia Antipolis.
- Ratzov, G., Collot, J.-Y., Sosson, M., & Migeon, S. (2010). Mass-transport deposits in the northern Ecuador subduction trench: Result of frontal erosion over multiple seismic cycles. *Earth and Planetary Science Letters*, 296(1–2), 89–102. <https://doi.org/10.1016/j.epsl.2010.04.048>
- Ratzov, G., Sosson, M., Collot, J.-Y., & Migeon, S. (2012). Late Quaternary geomorphologic evolution of submarine canyons as a marker of active deformation on convergent margins: The example of the South Colombian margin. *Marine Geology*, 315–318, 77–97. <https://doi.org/10.1016/j.margeo.2012.05.005>
- Reyes, P. (2013). *Évolution du relief le long des marges actives : Étude de la déformation Plio-Quaternaire de la Cordillère Côtière d'Équateur* (PhD thesis). Université de Nice-Sophia Antipolis.
- Robin, C., Samaniego, P., Le Pennec, J.-L., Fornari, M., Mothes, P., & van der Plicht, J. (2010). New radiometric and petrological constraints on the evolution of the Pichincha volcanic complex (Ecuador). *Bulletin of Volcanology*, 72(9), 1109–1129. <https://doi.org/10.1007/s00445-010-0389-0>
- Robin, C., Samaniego, P., Le Pennec, J.-L., Mothes, P., & van der Plicht, J. (2008). Late Holocene phases of dome growth and Plinian activity at Guagua Pichincha volcano (Ecuador). *Journal of Volcanology and Geothermal Research*, 176(1), 7–15. <https://doi.org/10.1016/j.jvolgeores.2007.10.008>
- Rosi, M., Landi, P., Polacci, M., Di Muro, A., & Zandomenighi, D. (2004). Role of conduit shear on ascent of the crystal-rich magma feeding the 800-year-BP Plinian eruption of Quilotoa Volcano (Ecuador). *Bulletin of Volcanology*, 66(4), 307–321. <https://doi.org/10.1007/s00445-003-0312-z>
- Rueda, H. (2005). *Erupciones plinianas del Holoceno en el Volcán Cerro Machín, Colombia. Estratigrafía, petrografía y dinámica eruptiva* (MSc thesis). Universidad Nacional Autónoma de México.

- Saalfeld, M. A., Kelley, D. F., & Panter, K. S. (2019). Insight on magma evolution and storage through the recent eruptive history of Cotopaxi Volcano, Ecuador. *Journal of South American Earth Sciences*, 93, 85–101. <https://doi.org/10.1016/j.jsames.2019.04.019>
- Sacchi, M., Insinga, D., Milia, A., Molisso, F., Raspini, A., Torrente, M. M., & Conforti, A. (2005). Stratigraphic signature of the Vesuvius 79 AD event off the Sarno prodelta system, Naples Bay. *Marine Geology*, 222–223, 443–469. <https://doi.org/10.1016/j.margeo.2005.06.014>
- Sage, F., Collot, J.-Y., & Ranero, C. R. (2006). Interplate patchiness and subduction-erosion mechanisms: Evidence from depth-migrated seismic images at the central Ecuador convergent margin. *Geologica*, 34(12), 997. <https://doi.org/10.1130/G22790A.1>
- Samaniego, P., Le Pennec, J.-L., Robin, C., & Hidalgo, S. (2011). Petrological analysis of the pre-eruptive magmatic process prior to the 2006 explosive eruptions at Tungurahua volcano (Ecuador). *Journal of Volcanology and Geothermal Research*, 199(1–2), 69–84. <https://doi.org/10.1016/j.jvolgeores.2010.10.010>
- Samaniego, P., Martin, H., Monzier, M., Robin, C., Fornari, M., Eissen, J.-P., & Cotten, J. (2005). Temporal evolution of magmatism in the Northern Volcanic Zone of the Andes: The geology and petrology of Cayambe Volcanic Complex (Ecuador). *Journal of Petrology*, 46(11), 2225–2252. <https://doi.org/10.1093/ptrology/egi053>
- Samaniego, P., Robin, C., Chazot, G., Bourdon, E., & Cotten, J. (2010). Evolving metasomatic agent in the Northern Andean subduction zone, deduced from magma composition of the long-lived Pichincha volcanic complex (Ecuador). *Contributions to Mineralogy and Petrology*, 160(2), 239–260. <https://doi.org/10.1007/s00410-009-0475-5>
- Santamaría, S., Telenchana, E., Bernard, B., Hidalgo, S., Beate, B., Córdova, M., & Narváez, D. (2017). Record of eruptions occurred in the northern Andes during the Holocene: New results obtained from the Potrerillos peatbog, Chiles-Cerro Negro Volcanic Complex. *Revista Politécnica (Escuela Politécnica Nacional – Quito)*, 39(2), 7–15.
- Schiano, P., Monzier, M., Eissen, J.-P., Martin, H., & Koga, K. T. (2010). Simple mixing as the major control of the evolution of volcanic suites in the Ecuadorian Andes. *Contributions to Mineralogy and Petrology*, 160(2), 297–312. <https://doi.org/10.1007/s00410-009-0478-2>
- Schindlbeck, J. C., Jegen, M., Freundt, A., Kutterolf, S., Straub, S. M., Mleneck-Vautravers, M. J., & McManus, J. F. (2018). 100-kyr cyclicity in volcanic ash emplacement: Evidence from a 1.1 Myr tephra record from the NW Pacific. *Scientific Reports*, 8(1), 4440. <https://doi.org/10.1038/s41598-018-22595-0>
- Siani, G., Michel, E., De Pol-Holz, R., DeVries, T., Lamy, F., Carel, M., et al. (2013). Carbon isotope records reveal precise timing of enhanced Southern Ocean upwelling during the last deglaciation. *Nature Communications*, 4(1), 2758. <https://doi.org/10.1038/ncomms3758>
- Sigurdsson, H., Carey, S., Palais, J. M., & Devine, J. (1990). Pre-eruption compositional gradients and mixing of andesite and dacite magma erupted from Nevado del Ruiz Volcano, Colombia in 1985. *Journal of Volcanology and Geothermal Research*, 41(1–4), 127–151. [https://doi.org/10.1016/0377-0273\(90\)90086-U](https://doi.org/10.1016/0377-0273(90)90086-U)
- Sun, S.-S., & McDonough, W. F. (1989). Chemical and isotopic systematics of oceanic basalts: Implications for mantle composition and processes. *Geological Society, London, Special Publications*, 42(1), 313–345. <https://doi.org/10.1144/GSL.SP.1989.042.01.19>
- Thouret, J. C., Cantagrel, J.-M., Robin, C., Murcia, A., Salinas, R., & Cepeda, H. (1995). Quaternary eruptive history and hazard-zone model at Nevado del Tolima and Cerro Machin volcanoes, Colombia. *Journal of Volcanology and Geothermal Research*, 66(1–4), 397–426. [https://doi.org/10.1016/0377-0273\(94\)00073-P](https://doi.org/10.1016/0377-0273(94)00073-P)
- Thouret, J.-C., Cantagrel, J. M., Salinas, R., & Murcia, A. (1990). Quaternary eruptive history of Nevado del Ruiz (Colombia). *Journal of Volcanology and Geothermal Research*, 41(1–4), 225–251. [https://doi.org/10.1016/0377-0273\(90\)90090-3](https://doi.org/10.1016/0377-0273(90)90090-3)
- Vallejo Vargas, S. (2011). *Distribución de las cenizas volcánicas holocénicas – tardías en la Costa del Ecuador* (PhD thesis). Escuela Politécnica Nacional.
- Van Daele, M., Meyer, I., Moernaut, J., De Decker, S., Verschuren, D., & De Batist, M. (2017). A revised classification and terminology for stacked and amalgamated turbidites in environments dominated by (hemi)pelagic sedimentation. *Sedimentary Geology*, 357, 72–82. <https://doi.org/10.1016/j.sedgeo.2017.06.007>
- Vatin-Pérignon, N., Goemans, P., Oliver, R. A., & Palacio, E. P. (1990). Evaluation of magmatic processes for the products of the Nevado del Ruiz Volcano, Colombia from geochemical and petrological data. *Journal of Volcanology and Geothermal Research*, 41(1–4), 153–176. [https://doi.org/10.1016/0377-0273\(90\)90087-V](https://doi.org/10.1016/0377-0273(90)90087-V)
- Vogel, S., & Märker, M. (2013). Modeling the spatial distribution of AD 79 pumice fallout and pyroclastic density current and derived deposits of Somma-Vesuvius (Campania, Italy) integrating primary deposition and secondary redistribution. *Bulletin of Volcanology*, 75(12), 778. <https://doi.org/10.1007/s00445-013-0778-2>
- Weller, D. J., de Porras, M. E., Maldonado, A., Méndez, C., & Stern, C. R. (2019). Petrology, geochemistry, and correlation of tephra deposits from a large early-Holocene eruption of Mentolat volcano, southern Chile. *Journal of South American Earth Sciences*, 90, 282–295. <https://doi.org/10.1016/j.jsames.2018.12.020>
- Wetzel, A. (2009). The preservation potential of ash layers in the deep-sea: The example of the 1991-Pinatubo ash in the South China Sea. *Sedimentology*, 56(7), 1992–2009. <https://doi.org/10.1111/j.1365-3091.2009.01066.x>
- White, W. M., Albarède, F., & Télouk, P. (2000). High-precision analysis of Pb isotope ratios by multi-collector ICP-MS. *Chemical Geology*, 167(3–4), 257–270. [https://doi.org/10.1016/S0009-2541\(99\)00182-5](https://doi.org/10.1016/S0009-2541(99)00182-5)
- Williams, M., Bursik, M. I., Cortes, G. P., & García, A. M. (2017). Correlation of eruptive products, Volcán Azufra, Colombia: Implications for rapid emplacement of domes and pyroclastic flow units. *Journal of Volcanology and Geothermal Research*, 341, 21–32. <https://doi.org/10.1016/j.jvolgeores.2017.05.001>
- Witt, C., Bourgeois, J., Michaud, F., Ordoñez, M., Jiménez, N., & Sosson, M. (2006). Development of the Gulf of Guayaquil (Ecuador) during the Quaternary as an effect of the North Andean block tectonic escape. *Tectonics*, 25(3), TC3017. <https://doi.org/10.1029/2004TC001723>
- Zeidler, J. A., & Pearsall, D. M. (1994). Regional Archaeology in Northern Manabí, Ecuador: Environment, cultural chronology, and prehistoric subsistence in the Jama river Valley. *University of Pittsburgh, Memoirs in Latin American Archaeology 8, Department of Anthropology*, J, 224.

## References From the Supporting Information

- Bronk Ramsey, C. (2009). Bayesian analysis of radiocarbon dates. *Radiocarbon*, 51(1), 337–360. <https://doi.org/10.1017/s0033822200033865>
- Etayo-Cadavid, M. F., Fred, C., Andrus, T., Jones, K. B., Hodgins, G. W. L., Sandweiss, D. H., et al. (2013). Marine radiocarbon reservoir age variation in *Donax obesulus* shells from northern Peru: Late Holocene evidence for extended El Niño. *Geology*, 41(5), 599–602. <https://doi.org/10.1130/g34065.1>
- Heaton, T., Köhler, P., Butzin, M., Bard, E., Reimer, R., Austin, W., et al. (2020). Marine20 – The marine radiocarbon age calibration curve (0–55,000 cal BP). *Radiocarbon*, 62(4), 779–820. <https://doi.org/10.1017/rdc.2020.68>

- Jones, K. B., Hodgins, G. W., Dettman, D. L., Andrus, C. F., Nelson, A., & Etayo-Cadavid, M. F. (2007). Seasonal variations in Peruvian marine reservoir age from pre-bomb *Argopecten purpuratus* shell carbonate. *Radiocarbon*, 49(2), 877–888. <https://doi.org/10.1017/s0033822200042740>
- Pyle, D. M. (1989). The thickness, volume and grain-size of tephra fall deposits. *Bulletin of Volcanology*, 51, 1–15. <https://doi.org/10.1007/bf01086757>
- Reimer, P., Austin, W., Bard, E., Bayliss, A., Blackwell, P., Bronk Ramsey, C., et al. (2020). The IntCal20 Northern Hemisphere radiocarbon age calibration curve (0–55 cal kBP). *Radiocarbon*, 62(4), 725–757. <https://doi.org/10.1017/rdc.2020.41>
- Stuiver, M., Reimer, P. J., & Reimer, R. W. (2021). CALIB 8.2. Retrieved from <http://calib.org>
- Taylor, J. R. (1997). *Introduction to error analysis, the study of uncertainties in physical measurements* (2nd ed.). University Science Books.
- Taylor, R. E., & Berger, R. (1967). Radiocarbon content of marine shells from the Pacific coasts of Central and South America. *Science*, 158(3805), 1180–1182. <https://doi.org/10.1126/science.158.3805.1180.b>